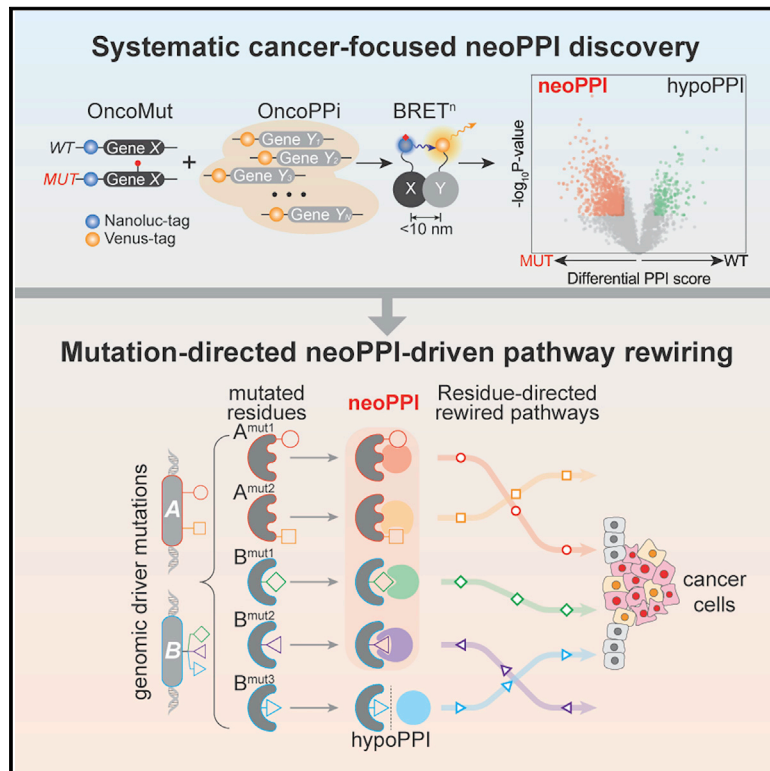# Systematic discovery of mutation-directed neo-protein-protein interactions in cancer

Graphical abstract

Authors

Xiulei Mo, Qiankun Niu,
Andrey A. Ivanov, ...,
Suresh S. Ramalingam, Gordon B. Mills,
Haian Fu

Correspondence

hfu@emory.edu

In brief

Pan cancer analysis unveils widespread driver-mutation-directed protein-protein interactions, informing variant-mediated rewiring of oncogenic programs and therapeutic approaches for precision medicine.

Highlights

- qHT-dS platform enables differential PPI mapping at single residue resolution

- Pan cancer analysis uncovers widespread driver-mutation-directed neoPPIs

- BRAF^{V600E}/KEAP1 neoPPI-rewired NRF2-pathway confers therapeutic vulnerability

- Annotated neoPPI dataset serves as resource to advance variant-specific target discovery

CelPress

Cell

CellPress

Resource

Systematic discovery of mutation-directed neo-protein-protein interactions in cancer

Xiulei Mo,[1,3,13] Qiankun Niu,[1,13] Andrey A. Ivanov,[1,2,3,13] Yiu Huen Tsang,[4] Cong Tang,[1,5] Changfa Shu,[1,6] Qianjin Li,[1] Kun Qian,[1] Alafate Wahafu,[1,7] Sean P. Doyle,[1] Danielle Cicka,[1] Xuan Yang,[1,2] Dacheng Fan,[1] Matthew A. Reyna,[8] Lee A.D. Cooper,[9] Carlos S. Moreno,[3,8,10] Wei Zhou,[10,11] Taofeek K. Owonikoko,[11] Sagar Lonial,[11] Fadlo R. Khuri,[11,12] Yuhong Du,[1,2,3] Suresh S. Ramalingam,[3] Gordon B. Mills,[4] and Haian Fu[1,2,3,11,14,*]

[1]Department of Pharmacology and Chemical Biology, Emory University School of Medicine, Atlanta, GA 30322, USA
[2]Emory Chemical Biology Discovery Center, Emory University School of Medicine, Atlanta, GA 30322, USA
[3]Winship Cancer Institute of Emory University, Atlanta, GA 30322, USA
[4]Division of Oncologic Science, Oregon Health Sciences University School of Medicine, Portland, OR 97239, USA
[5]Department of Urology, The First Affiliated Hospital, Medical School of Xi'An Jiaotong University, Xi'an, Shannxi 710061, PRC
[6]Department of Gynecology, The Third Xiangya Hospital of Central South University, Changsha, Hunan 410013, PRC
[7]Department of Neurosurgery, the First Affiliated Hospital of Xi'An Jiaotong University, Xi'an, PRC
[8]Department of Biomedical Informatics, Emory University School of Medicine, Atlanta, GA 30322, USA
[9]Department of Pathology, Northwestern University Feinberg School of Medicine, Chicago, IL, USA
[10]Department of Pathology and Laboratory Medicine, Emory University School of Medicine, Atlanta, GA 30322, USA
[11]Department of Hematology and Medical Oncology, Emory University, Atlanta, GA 30322, USA
[12]Department of Internal Medicine, Division of Hematology and Oncology, American University of Beirut, Beirut, 1107-2020, Lebanon
[13]These authors contributed equally
[14]Lead contact
*Correspondence: hfu@emory.edu
https://doi.org/10.1016/j.cell.2022.04.014

SUMMARY

Comprehensive sequencing of patient tumors reveals genomic mutations across tumor types that enable tumorigenesis and progression. A subset of oncogenic driver mutations results in neomorphic activity where the mutant protein mediates functions not engaged by the parental molecule. Here, we identify prevalent variant-enabled neomorph-protein-protein interactions (neoPPI) with a quantitative high-throughput differential screening (qHT-dS) platform. The coupling of highly sensitive BRET biosensors with miniaturized co-expression in an ultra-HTS format allows large-scale monitoring of the interactions of wild-type and mutant variant counterparts with a library of cancer-associated proteins in live cells. The screening of 17,792 interactions with 2,172,864 data points revealed a landscape of gain of interactions encompassing both oncogenic and tumor suppressor mutations. For example, the recurrent BRAF V600E lesion mediates KEAP1 neoPPI, rewiring a BRAF^{V600E}/KEAP1 signaling axis and creating collateral vulnerability to NQO1 substrates, offering a combination therapeutic strategy. Thus, cancer genomic alterations can create neo-interactions, informing variant-directed therapeutic approaches for precision medicine.

INTRODUCTION

Genomic mutation data provide a compelling structural framework to infer functional significance and to nominate potential cancer driver genes and therapeutic targets (Hahn et al., 2021; Lawrence et al., 2014; Martínez-Jiménez et al., 2020; Cancer Target Discovery and Development Network et al., 2010). However, it is emerging that different driver mutations, even in the same cancer gene, can be functionally distinct with different clinical significance (Burd et al., 2014; Chang et al., 2016; Menzies et al., 2012; Vivanco et al., 2012; Westcott et al., 2015). Therefore, translating this cancer mutation information into therapeutic applications at mutated amino acid level presents both an unprecedented challenge and opportunity for

identifying mutant-allele-specific targets, biomarkers, and therapeutic vulnerabilities.

Some mutations are found in driver genes that encode actionable targets, but the majority are located in genes without direct connection to known drugs, or in genes encoding "undruggables" such as adaptor proteins or tumor suppressors (Ivanov et al., 2013; Vogelstein et al., 2013). These "undruggable" proteins exert their functions primarily through interactions with other cellular components through protein-protein interaction (PPI) networks (Arkin et al., 2014; Ivanov et al., 2013; Li et al., 2017). Thus, understanding how cancer driver mutations are integrated within cellular signaling networks through altered PPIs may lead to potential strategies for pathway perturbation to reach the "undrugged" space of the cancer genome (Figure 1A).
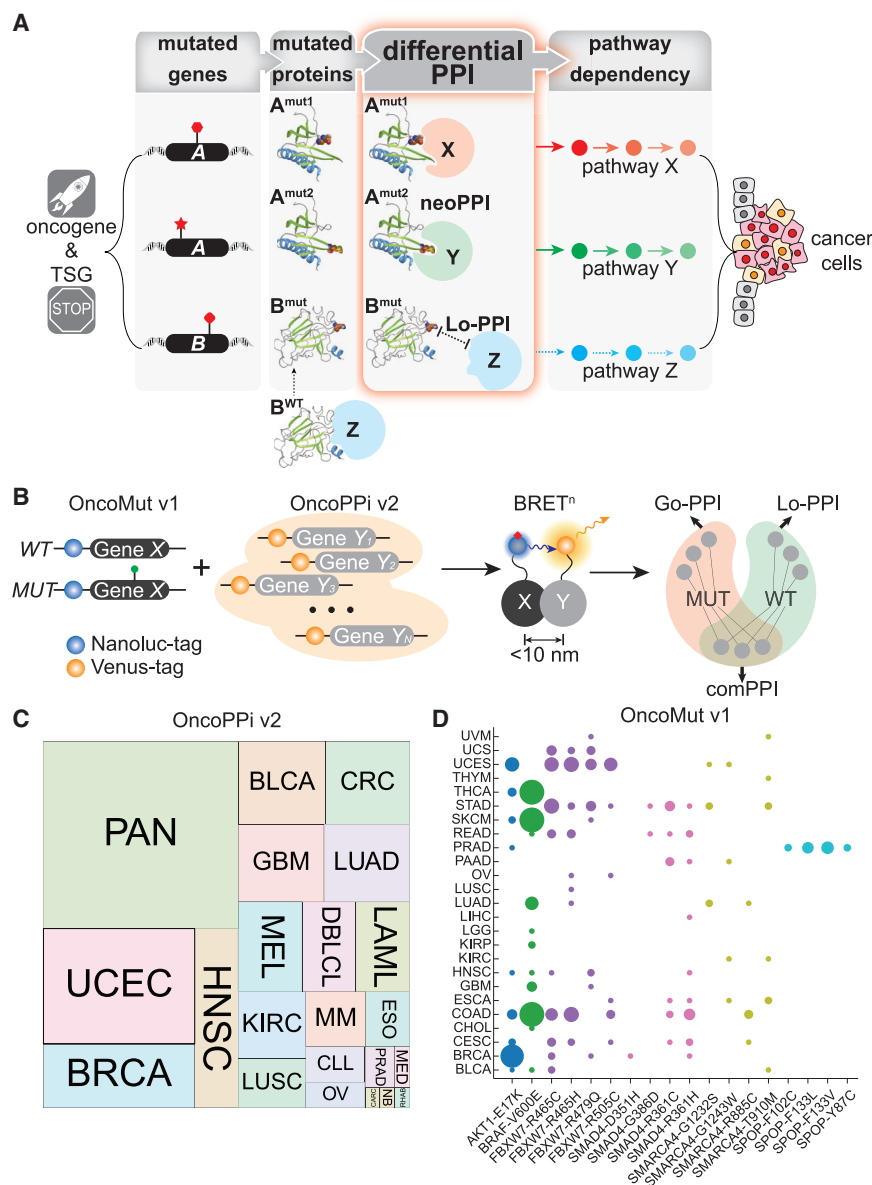
Figure 1. Schematic illustration of qHT-dS platform for systematic differential PPI discovery

(A) Cancer driver mutations are translated to mutated residues that may lead to mutation-directed differential PPIs and pathway rewiring.

(B) Components of the qHT-dS platform to identify mutation enhanced Go-PPIs, mutation-reduced Lo-PPI, and common PPIs (STAR Methods).

(C) Square pie chart illustrating the tumor types by the distribution of genes in OncoPPi v2 library.

(D) Bubble plot showing the tumor driver mutations and their frequency and tumor lineage distributions in OncoMut v1 library.

See also Figures S1 and S2.

Missense mutations are common genetic alterations contributing to tumorigenesis. The mutant (MUT) alleles may create neo-epitopes on the encoded proteins (Figure 1A). Such mutations may alter the intrinsic properties of the encoded proteins. It is also possible that those neo-epitopes may generate docking sites to induce neo-interactions or act as impediments to weaken existing interactions. Such neo-epitope-triggered differential PPIs (Df-PPI) may dictate rewired oncogenic programs that underlie the dysregulated growth and spread of tumor cells and may reveal much-needed tumor-specific molecular targets for therapeutic intervention. However, the prevalence and spectrum of neo-interactions triggered by mutations in oncogenes and tumor suppressors remains to be established. How to systematically discover those mutated residue-directed PPIs in a physiologically relevant cellular environment poses a major challenge.

To address these challenges, we established a NanoLuc luciferase-based bioluminescence resonance energy transfer (BRET^n) technology-based differential PPI discovery platform that allows comparative screening of wild-type (WT) and MUT allele counterparts for the detection of differential interactions with cancer-associated proteins in live mammalian cells (Figures 1B and S1). The high throughput and quantitative nature of the technology, termed quantitative high-throughput differential screening (qHT-dS), enabled the systematic identification of differential WT and MUT interaction proteins for 32 alleles from the examination of 17,792 pairs of potential PPIs. Analysis of high-stringency Df-PPI datasets revealed widespread gain of interactions induced by missense mutations of both oncogenes and tumor suppressors. Examination of mutation-directed neomorph PPIs (neoPPI) revealed potential alternative mechanisms and signaling pathways for well-studied mutated forms of oncogenes and tumor suppressors. The BRAF^{V600E}/KEAP1 interaction was selected for validation using a panel of orthogonal assays that advanced it to a validated neoPPI status. This neoPPI redirects BRAF^{V600E} to upregulate NRF2-mediated redox signaling while exposing a collateral therapeutic vulnerability for a combination strategy. Our qHT-dS platform enables the accelerated discovery of Df-PPIs at single mutated residue resolution with the resultant dataset serving as a resource for the biomedical community for precision oncology approaches.

RESULTS

Cancer-associated gene expression library for focused PPI screening

To identify molecular rewirings emanating from recurrently mutated residues encoded by genomic alterations, we sought to establish the connectivity of mutated residues and proteins

CellPress
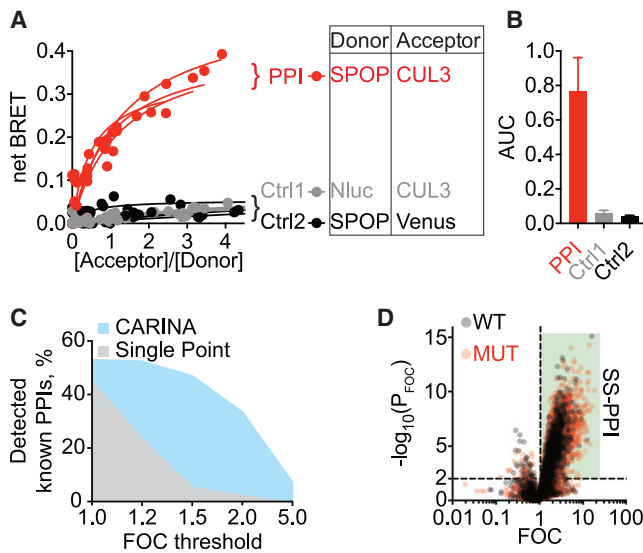
Figure 2. Evaluation of qHT-dS platform performance

(A) Representative BRET saturation curves from qHT-dS using a known PPI, SPOP ^{WT}/CUL3, as an example.

(B) AUC analysis of the BRET saturation curves.

(C) Positive discovery rate of the known WT PPIs using CARINA comparing to the single point analysis.

(D) Identification of statistically significant (SS) positive PPIs for both WT and MUT.

with defined cancer-associated proteins for focused comparative examinations. For this purpose, we constructed a cancer-associated gene expression library, termed the OncoPPi v2 library (Figures 1C and S2; Table S1), consisting of 556 distinct human WT protein-coding ORFs to search for interaction partners of driver mutations.

To select human cancer mutant alleles for Df-PPI discovery, we established a collection of oncogenic mutation expression vectors, termed the OncoMut library. For the systematic comparative study of driver mutations, we focused initially on recurrent mutations in two well-defined oncogenes and four frequently mutated tumor suppressor genes with 24 alleles from diverse tumor lineages (Figure 1D). These mutations were nominated based on their disease prevalence and their surface exposure potential for increased likelihood of creating neo-interaction epitopes (Kamburov et al., 2015). The OncoMut library contains mutations in oncogenes AKT1 and BRAF; tumor suppressors Speckle type BTB/POZ protein (SPOP), F-box, and WD repeat domain containing 7 (FBXW7); and transcription regulators, mothers against decapentaplegic homolog 4 (SMAD4), and SWI/SNF-related, matrix-associated, actin-dependent regulators of chromatin, subfamily A, member 4 (SMARCA4). The selected mutations that represent diverse protein classes in the OncoMut library (Figure 1D), together with the OncoPPi library (Figure 1C), serve as the foundation for Df-PPI discovery.

The qHT-dS platform for comparative WT and MUT PPI profiling

To systematically discover Df-PPIs in live cells, a differential screening platform, qHT-dS, was established (Figures 1B and

S1). It is enabled by using BRET^n-based ultra-high-throughput PPI screening technology in a 1536 well plate format (Mo and Fu, 2016; Mo et al., 2016) (Figure S1A). Briefly, the WT and MUT proteins, genetically tagged with Nanoluc-luciferase (NLuc) as a BRET^n donor, were tested against each protein in the OncoPPi v2 library that are tagged with Venus as a BRET^n acceptor in a parallel fashion (Figure S1B). Due to the stringent proximity requirement (<10 nm) for a positive BRET^n signal, the identified PPIs generally reflect direct interactions in protein complexes. Upon substrate addition, three readouts were generated that capture: (i) luminescence from NLuc-fusions, (ii) fluorescence from Venus fusion, and (iii) the ratiometric BRET signal from the Venus/NLuc emissions. The highly sensitive and multiplexed PPI signal detection of qHT-dS with streamlined monitoring of test protein expression levels for BRET signal calibration allows for large-scale screening of PPIs in live cells (Figure S1C).

With the automated qHT-dS workflow (Figure S1), we systematically tested 24 WT and MUT alleles for their binary interactions with 556 cancer-associated proteins in the OncoPPi v2 library in HEK293T cells. A total of 13,344 interactions were examined with eight points of titration combinations in four replicates for each PPI's BRET saturation curve (Table S2A), generating a total of 1,469,376 data points. Such primary PPI signals were normalized to the luminescence signal for NLuc-tagged MUT or WT expression and to the fluorescence signal for expression of Venus-tagged OncoPPi genes. Ratiometric data for each PPI were calibrated with protein expression levels for each partner, enabling quantitative comparative assessment of each PPI. To ensure a rigorous statistical evaluation of the qHT-dS data, the comparative analysis of rewired interactions (CARINA) algorithm was developed and implemented to quantify the intensity of interaction signals (Figure 2A). The fold-over-control (FOC) data were integrated with p value analysis of the area under curve (AUC) values (P_{FOC}) from the BRET saturation curves for comparative studies to identify positive WT and MUT PPIs (Figures 2B–2D).

Through CARINA analysis, a total of 55,600 BRET saturation curves were built for each PPI and its corresponding empty donor/acceptor controls. In contrast to the single point protein expression binary PPI mapping (Li et al., 2017), qHT-dS incorporates variations in protein expression. With cutoffs of FOC ≥ 1.2 and P_{FOC} ≤ 0.01, CARINA identified more than 50% of known WT PPIs, whereas a lower FOC cutoff below 1.2 only slightly increased the number of known PPI detected in the screening (Figure 2C). Therefore, FOC ≥ 1.2 and P_{FOC} ≤ 0.01 were used as the primary threshold to define statistically significant (SS) PPIs. With these parameters, a total of 8,839 primary positive PPIs were identified (Figure 2D; Table S2B). These positive PPIs serve as a candidate pool for further evaluation to identify differential PPIs.

Systematic analysis to prioritize differential PPIs

To identify mutant-driven Df-PPIs, we performed the comparative analysis according to the FOC values of WT and MUT PPI profiles. To differentiate gain of interactions (Go-PPI) from loss of interactions (Lo-PPI), the difference between WT and MUT PPI curves were calculated to obtain differential scores (DS)
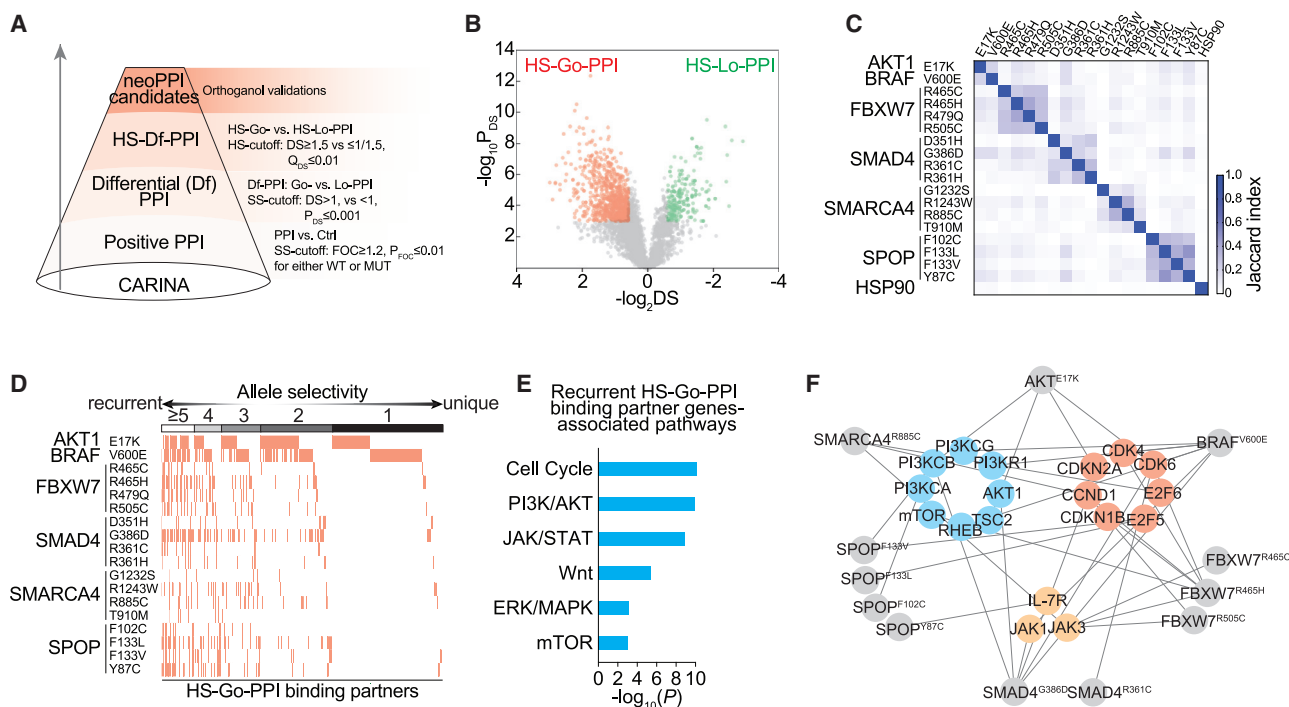
Figure 3. Systematic analysis to prioritize differential PPI to advance neoPPI candidates

(A) Flow chart of differential PPI identification and neoPPI candidate prioritization.

(B) Volcano plot of the differential score versus p values for each WT/MUT PPI pair shows the identified HS-Go- and HS-Lo-PPI.

(C) Similarity analysis of HS-Go-PPI binding partners between alleles.

(D) Clustering analysis reveals recurrent and unique HS-Go-PPI binding partners.

(E) Commonly rewired pathways that are significantly enriched for the recurrent HS-Go-PPI binding partners from the pathway analysis.

(F) Go-PPI network links various driver mutations of diverse genes with commonly rewired oncogenic pathways, with supporting evidence from qHT-dS and GST pulldown validation.

and the corresponding p values (P_{DS}) (Figure 3A; Table S2B). Based on DS and P_{DS}, 864 differential Go-PPI (DS > 1 and $P_{DS} \leq 0.001$) and 172 differential Lo-PPIs (DS < 1, and $P_{DS} \leq 0.001$) were identified. To prioritize PPIs for confirmatory studies, the adjusted p value (Q_{DS}) cutoff of $Q_{DS} \leq 0.01$ and high stringent (HS) cutoffs of DS $\geq$ 1.5 or DS $\leq$ 1/1.5, indicating at least 50% difference between WT and MUT PPI signals, were applied to compile the HS-Go-PPI and HS-Lo-PPI groups of 359 and 13 PPIs, respectively (Figures 3A and 3B; Table S2B). These 372 HS-differential PPIs were utilized to assess the specificity and nature of allele-dependent interactions.

The qHT-dS design with built-in titration of interaction pairs allows for the detection of PPIs near or at the endogenous protein levels (Figure S3A) (Mo et al., 2016). The CARINA analysis was used to capture a subset of HS-Go-PPI data from the lowest expression levels of both donor and acceptor proteins, revealing 267 of 359 HS-Go-PPI positive PPIs under these low protein expression conditions ($FOC_{(MUT)/(WT)} > 2$, $p \leq 0.001$) (Table S2B).

Different gene products, or even different alleles from the same gene, showed remarkable divergence in their interaction partners from an analysis of their HS-Go-PPI profiles (Figure 3C). For example, less than 10% of overlapping Go-PPI partners were found for mutations in two E3 ligase adaptor proteins, SPOP and FBXW7. The fractions of shared partners for G386D

versus D351H SMAD4 alleles and F102C versus F133V SPOP alleles were 13% and 30%, respectively, exhibiting mutation-specific interactions. Surprisingly, mutations at the same site showed differential interactions in a residue-dependent manner. As an example, 62% of SPOP F133L partners were different from those of F133V. Such mutant-allele-specific interactions were unlikely due to association with the general chaperone function of heat shock protein 90 (HSP90), although a number of disease mutants show increased interaction with HSP90 (Oughtred et al., 2019; Sahni et al., 2015). Indeed, only minimal overlap (1.4 ± 0.9%) between HS-Go-PPI and HSP90 known PPI partners was noted (Figure 3C). These results highlight the specificity of mutant-allele-mediated Go-PPIs and potential allele-dependent tumor heterogeneity at the protein connectivity level.

To gain insights into allele-driven oncogenic programs, allele selectivity for each partner was examined (Figure 3D). In total, 35% of HS-Go-PPI partners interact with 3 or more alleles, implicating shared oncogenic pathways by different mutations. These recurrent HS-Go-PPI partners function in core growth regulatory pathways (Figure 3E; Table S2C). In support of this notion, an orthogonal affinity GST pulldown assay of Df-PPIs showed evidence of engagement of various mutated residues in common pathways, such as cell cycle, PI3K/AKT/mTOR and JAK/STAT pathways, offering a mechanistic basis for the oncogenic
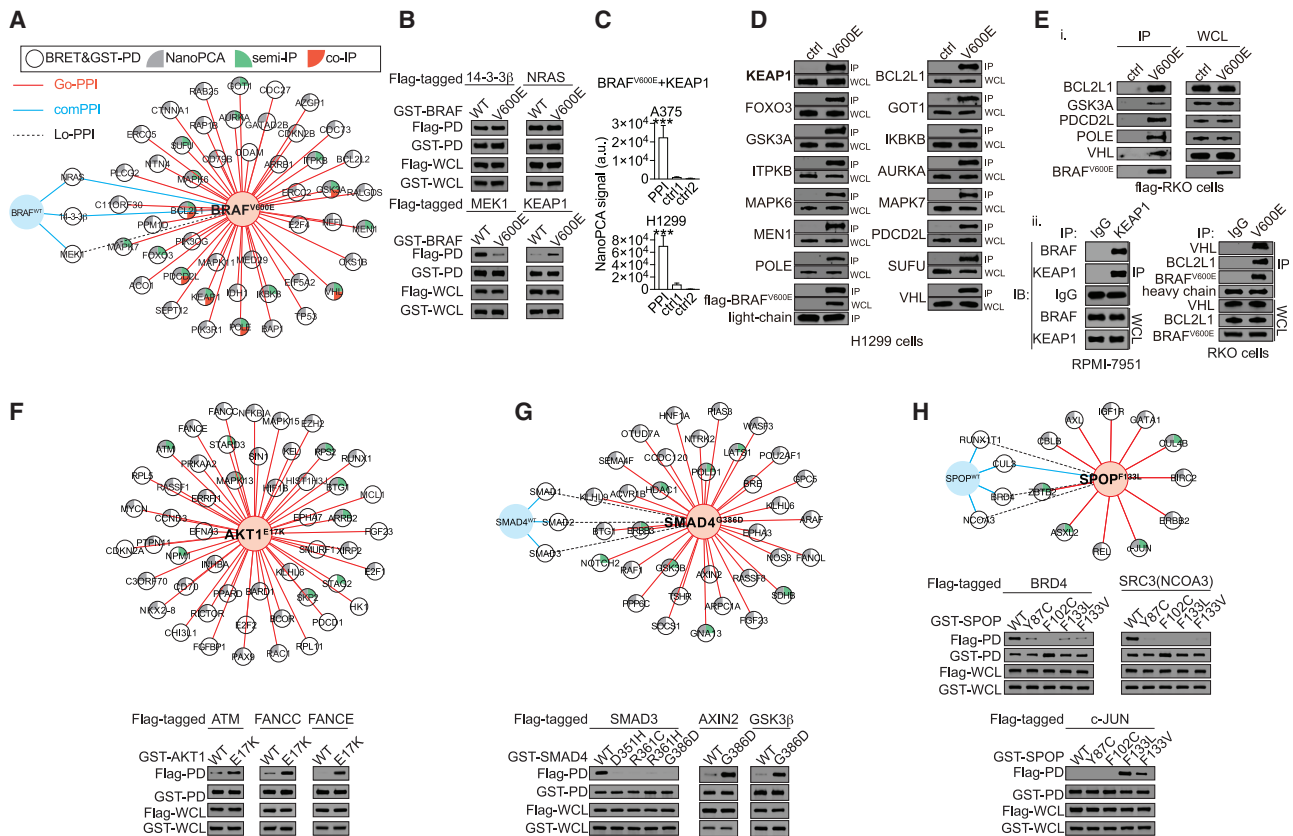
Figure 4. neoPPI candidates induced by mutations of tumor suppressors and oncogenes

(A) Spoke diagram of BRAF^{V600E} allele-selective neoPPI hubs with experimental evidence from BRET, GST pulldown (PD), NanoPCA, semi-IP of epitope-tagged mutant with endogenous binding partners, and co-IP of endogenous mutant and binding partner complexes.

(B) GST pulldown results of the selected Go-PPI, comPPI, and/or Lo-PPI in HEK293T cell overexpressing the GST-tagged BRAF^{V600E} and its comPPI binding partner Venus-Flag-tagged 14-3-3β and NRAS, Lo-PPI with MEK1, and neoPPI with KEAP1.

(C) NanoPCA results of BRAF^{V600E}/KEAP1 PPI in A375 and H1299 cells. The data are presented as mean ± SD from four replicates of the NanoPCA screen. *** p ≤ 0.001.

(D) Semi-IP of flag-BRAF^{V600E} and endogenous binding partners, such as KEAP1, in H1299 cells. H1299 cells expressing flag-BRAF^{V600E} or empty-vector were subjected to anti-flag immunoprecipitation and SDS-PAGE and western blot analysis with respective antibodies as indicated.

(E) Co-immunoprecipitation (co-IP) of endogenous BRAF^{V600E} and binding partners in cancer cell lines. (i) Co-IP of endogenous BRAF^{V600E} in an isogenic genetically engineered RKO cells with flag-tag knockin at the endogenous BRAF^{V600E} loci (flag-RKO: V600E CBP-DYKDDDDK/V600E/+). Parental untagged RKO cells were used as control. (ii) Co-IP of KEAP1 with BRAF^{V600E} in RPMI-7951 cells carrying V600E mutation (left); and co-IPs of endogenous untagged BRAF^{V600E} with VHL and BCL2L1 in parental RKO cells. The IP complexes were precipitated with indicated antibodies with IgG as control.

(F–H) (upper) Spoke diagram of (F) AKT1^{E17K}, (G) SMAD4^{G386D}, and (H) SPOP^{F133L} allele-selective neoPPI hubs with experimental evidence as indicated; (lower) GST pulldown validation of selected PPIs as indicated.

See also Data S1.

function of those driver mutations (Figure 3F; Data S1). Additionally, the majority of HS-Go-PPI partners (65%) interact with one or two alleles, suggesting that these partners and corresponding pathways could be specifically altered in cancers harboring certain mutations (Figure 3D).

Orthogonal experimental evaluation of neoPPI candidates

To gather further experimental evidence to advance the characterization of mutation-directed differential PPIs, we sampled the HS-Df-PPI dataset for secondary verification in an affinity-based GST pulldown assay in mammalian cells. In total, 265 of 325 PPIs showed differential binding signals, representing 82% of HS-Df-

PPIs with supporting evidence from both homogenous BRET assay and affinity GST pulldown assay (Figure 4; Data S1). These double positive Df-PPIs were used as mutation-enabled neoPPI candidates. Orthogonal PPI assays were performed for selected mutation-enabled neoPPIs for their biological relevance.

As a case study to demonstrate neo-interactions in disease-relevant cellular context, BRAF^{V600E}-mediated neoPPI candidates (Figure 4A; Table S3A) were examined in melanoma, lung, and colon cancer cells where BRAF^{V600E} defines a subpopulation of patients, with three complementary assays. (i) A NanoPCA assay was used to confirm BRAF^{V600E}-neoPPIs in cancer cells near endogenous expression levels (Mo et al., 2017), providing evidence for the interaction of 44 and 38 binding

partners with BRAF^{V600E} in A375 melanoma cells and H1299 lung cancer cells, respectively (Figures 4A and 4C; Table S4). (ii) The flag-tagged BRAF^{V600E} was used to examine its interaction with endogenous binding partners. Fifteen endogenous partners were detected in the flag-BRAF^{V600E} immunocomplexes in lung cancer cells (Figure 4D). Five neoPPIs were further confirmed with an endogenous flag-V600E co-IP study in a colon cancer cell line (Figure 4Ei). (iii) co-IP quality antibodies were utilized to demonstrate endogenous BRAF^{V600E}complexes with VHL, BCL2L1, and KEAP1 in a native state of patient-derived cancer cells harboring BRAF^{V600E} (Figure 4Eii). In this way, each candidate neoPPI for BRAF^{V600E} was annotated with various supporting evidence in relevant cancer cells summarized in the spoke diagram (Figure 4A).

Similarly, AKT1^{E17K} neo-interactions were examined in MCF7 breast cancer cells, SMAD4^{G386D} PPIs were tested in HCT116 colon cancer cells, and SPOP^{F133L} partners were evaluated in C4-2 prostate cancer cells for their interactions with endogenous partners (Figures 4F-4H; Data S1 Figures iii–v). The spoke diagrams of the AKT1^{E17K}, SMAD4^{G386D}, and SPOP^{F133L} neoPPIs were shown with experimental evidence (Figures 4F–4H).

neoPPI Candidates inform hypothesis for mutations of tumor suppressors and oncogenes

The extensive mutation-affected PPIs suggest potential reprogramed pathways in cancer (Figures 3 and 4). To begin to explore Df-PPI data-suggested pathways for hypothesis testing, we examined identified PPI hubs of both tumor suppressor and oncogene proteins. Tumor suppressor genes were generally believed to enable tumorigenesis through loss-of-function mutations, which impair their tumor-suppressive functions (Cheng et al., 2021). Unexpectedly, the Df-PPI data showed that tumor suppressor mutations exhibited both Lo-PPIs and Go-PPIs with a different set of cancer-associated proteins, implying a possible mechanism for tumor suppressors to gain a neomorph activity through neo-interactions. For instance, the enhanced interaction of SMAD4^{G386D} with GSK3β may allow SMAD4^{G386D} to gain an ability to impact the GSK3β-regulated Wnt/β-catenin pathway (Data S1 Figure iv). SPOP^{F133L}, a tumor suppressor frequently mutated in prostate cancer, not only lost the interaction with known WT binding partners, such as BRD4 and NCOA3 (SRC-3), but also enhanced interaction with different partners, such as c-JUN (Figure 4H). The SPOP^{F133L}/c-JUN neoPPI supports the hypothesis that SPOP mutations may potentially engage the c-JUN pathway to drive AP-1-mediated oncogenic program (Data S1 Figure v). Such gain-of-interaction features were detected for other tumor suppressor mutations, such as FBXW7 and SMARCA4 (Data S1 Figure vi). These tumor suppressor variant-driven Go-PPIs illustrate another dimension of the complexity underpinning the role of tumor suppressors in enabling tumorigenesis and cancer progression, which warrants further examination.

Our qHT-dS data also showed that driver mutations of oncogenic kinases, such as AKT1^{E17K} and BRAF^{V600E}, enabled interactions with multiple binding partners, which may rewire oncogenic pathways and suggest alternative pathway perturbation approaches (Figure 4). For example, our screening revealed 51 allele-selective binding partners for AKT1^{E17K} (Figure 4F; Data S1 Figure iii, Table S3B), a mutation frequently activated in various cancers (Carpten et al., 2007; Chen et al., 2020). The AKT1^{E17K}-mediated interactions were supported by additional datasets, including binding with endogenous partners in breast cancer cells, shared subcellular localizations, and the existence of defined AKT1 phosphorylation motifs of a subset of partners (Figure 4F; Data S1 Figure iii; Table S3B and S5A). Among identified Go-PPIs, the E17K mutation appeared to enhance interaction of AKT1 with DNA damage response (DDR) proteins, such as ATM and FANCC/E (Figure 4F), which raised the possibility that AKT1^{E17K} may alter response of cells to DNA damage and repair (Ceccaldi et al., 2016; Garcia-Higuera et al., 2001; Matsuoka et al., 2007; Shiloh and Ziv, 2013). The positive correlation of the AKT1^{E17K} status with enhanced cells resistance to DNA damage signals supports future testing of the hypothesis that AKT1^{E17K} may regulate DDR through neoPPI with ATM (Data S1 Figure iii) (Boehme et al., 2008; Kandel et al., 2002; Viniegra et al., 2005). Similarly, the hot-spot mutation, V600E, enabled the interaction of BRAF with protein partners beyond the RAS/MEK signaling cascade (Karoulia et al., 2017). We confirmed common PPIs with NRAS and 14-3-3β and Lo-PPI with MEK1 for BRAF^{V600E} compared with the WT counterpart (Figures 4A and 4B), supporting the reported model of BRAF^{V600E} regulated signaling (Haling et al., 2014). We also identified 47 V600E-enhanced PPI candidates (Table S3A), significantly expanding the BRAF^{V600E}-mutation allele-mediated oncogenic pathways (Figures 4A-E; Data S1 Figures i and ii). These examples showed the potential of the Df-PPI dataset to suggest neoPPI-mediated oncogenic pathways as a launching point for biological and therapeutic hypothesis testing.

Neo-interaction of BRAF^{V600E} with KEAP1 enables oncogenic rewiring and its collateral vulnerability

To illustrate the utility of the discovered neoPPI candidates to inform oncogenic mechanisms for functional evaluation and therapeutic intervention, we examined BRAF^{V600E}-enabled neo-interactions and selected the BRAF^{V600E}/KEAP1 neoPPI for functional studies.

Bioinformatics analysis of BRAF^{V600E}-associated interactions

We assessed the potential biological significance of the BRAF^{V600E}-induced neo-interactions with database mining and annotation. Mutual exclusivity analysis was used to infer functional connectivity in cancer patients (Ciriello et al., 2012) and revealed that alterations in 45 of 47 neoPPI binding partners showed mutual exclusivity with BRAF^{V600E} in thyroid, melanoma, or colon cancers and 39 binding partners colocalized with BRAF (Figure S4, Table S5B). Genetic perturbation analysis with the DepMap dataset showed that V600E harboring cells had significantly lower cell fitness scores than that of WT cells (p value ≤ 0.05) upon knocking down/out of 9 V600E-neoPPI partners, such as KEAP1 (Table S5B). Lastly, from the analysis of therapeutic response profiles of the CTRP dataset, the drug sensitivity of V600E harboring cell lines to vemurafenib, a BRAF^{V600E} inhibitor, showed significant correlation (Pearson correlation coefficient |R| ≥ 0.3 and p value ≤ 0.05) with mRNA or protein expression levels of 14 genes, such as aconitase 1 (ACO1) (Table S5B). These data add evidence in support of the functional importance
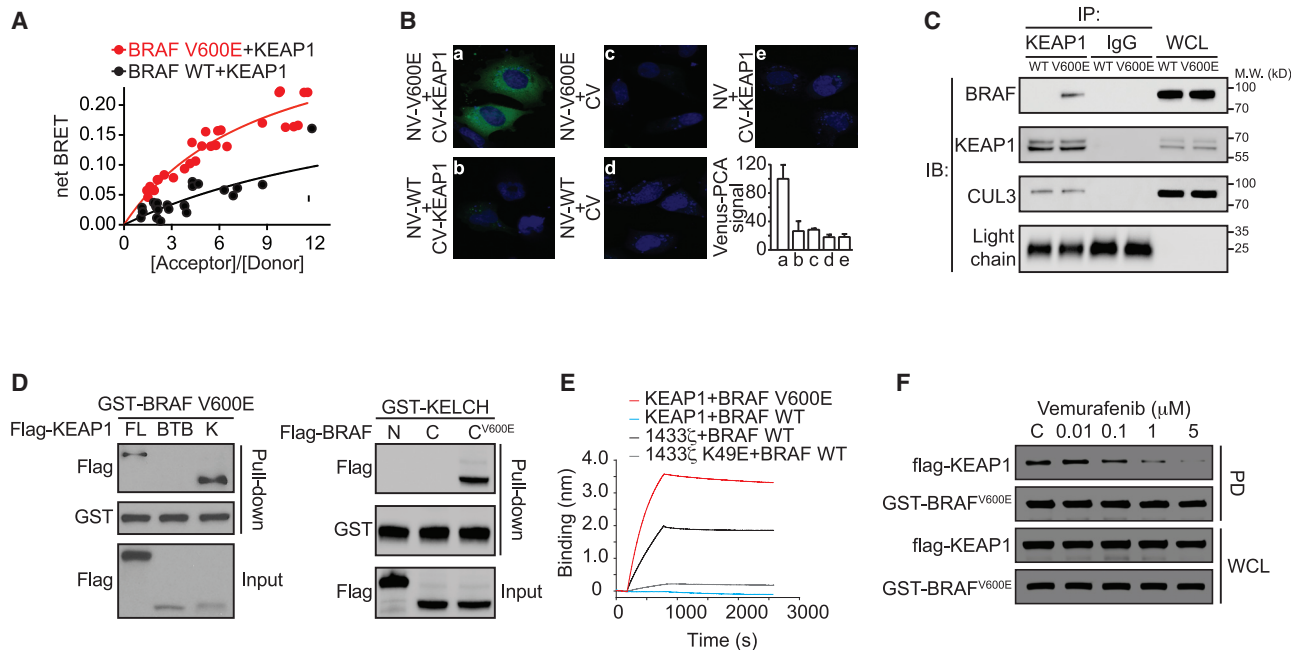
Figure 5. Validation of BRAF^{V600E} interaction with KEAP1

(A) BRET saturation curve of BRAF^{V600E}/KEAP1 neoPPI from qHT-dS. The data are presented by combining four replicates from the primary qHT-dS in HEK293T cells.

(B) Venus-PCA shows the cytoplasm localization of BRAF^{V600E}/KEAP1 neoPPI using CHL-1 melanoma cell line, transfected with N-Venus-tagged BRAF WT or V600E and C-Venus-tagged KEAP1. Green: reconstituted Venus signal. Blue: nuclear stained with Hoechest. Venus-PCA signal was presented as the normalized fluorescence intensity.

(C) Endogenous interaction of BRAF^{V600E} with KEAP1. The BRAF^{V600E}/KEAP1 complex was co-IPed with KEAP1 antibody from a pair of isogenic colon cancer cells, parental RKO cells harboring BRAF^{V600E} alleles and isogenic V600E-knockdown RKO (+/-/-) counterparts, with IgG as control.

(D) GST pulldown assay with BRAF and KEAP1 domain fragments. Cell lysate from HEK293T cells expressing the corresponding truncation constructs were subjected to GST pulldown and western blot as indicated.

(E) BLI validation of the direct interaction between KEAP1 KELCH domain and BRAF^{V600E} kinase domain using human recombinant proteins. Interaction between 14-3-3ζ and BRAF^{WT} kinase domain was used as positive control, with 14-3-3ζ^{K49E} and BRAF^{WT} as negative control.

(F) Effect of BRAF^{V600E} kinase inhibition by vemurafenib on BRAF^{V600E}/KEAP1 neoPPI. HEK293T cells transfected with GST-BRAF^{V600E} and Venus-flag-KEAP1 were treated with vemurafenib at indicated concentrations for 24 h.

See also Data S1ii.

of BRAF^{V600E}-neoPPIs for tumor proliferation, survival, or therapeutic response. For example, the BRAF^{V600E}-enhanced interactions with ACO1 and KEAP1 suggest that BRAF^{V600E} may regulate ACO1-driven iron homeostasis and KEAP1-driven ROS homeostasis (Data S1 Figure ii). These data highlight possible BRAF^{V600E}-rewired pathways enabled by the uncovered neo-PPIs, such as the BRAF^{V600E}/KEAP1 neo-interaction.

Neo-interaction of BRAF^{V600E} with KEAP1

Based on multiple tiers of evidence from statistical analysis, orthogonal assays in the context of relevant cancer types, and genomic perturbation data, we postulated that the mutated BRAF^{V600E} created a neo-epitope with enhanced affinity to KEAP1, which may affect ROS response through modulating the NRF2-mediated pathway (Jaramillo and Zhang, 2013; Sporn and Liby, 2012). To test this hypothesis, we further assessed this neoPPI with a panel of complementary biochemical and cellular assays.

Consistent with the qHT-dS readouts (Figure 5A), BRAF^{V600E} showed significantly higher interaction signals than the WT and other BRAF mutants with KEAP1 in a GST pulldown assay (Fig-ures 4 and S5A). This neo-interaction was demonstrated in live cells showing cytoplasmic localization with the Venus-PCA assay (Figure 5B), and under endogenous cellular conditions with co-IP studies in a pair of isogenic cell lines (Figure 5C) and a panel of patient-derived BRAF^{V600E} melanoma cell lines (Figure 4E; Data S1 Figure ii), supporting its presence under physiological conditions. Truncation studies suggested the involvement of the kinase domain of BRAF^{V600E} and the KELCH domain of KEAP1 for their association (Figure 5D). This neo-interaction appears to be direct and reversible. With the purified proteins in a Biolayer Interferometry (BLI) analysis, the kinase domain of BRAF^{V600E}, but not that of WT, exhibited direct binding BLI signals to the KEAP1 KELCH domain (Figure 5E). Treatment of BRAF^{V600E} carrying cells with vemurafenib attenuated the BRAF^{V600E}/KEAP1 interaction in a dose-dependent manner (Figure 5F). Together, these data strongly support a physiologically relevant neoPPI, BRAF^{V600E}/KEAP1.

BRAF^{V600E}/KEAP1 neoPPI-directed NRF2 signaling

These data suggested an undescribed function of the mutated BRAF as a regulator of the KEAP1-mediated redox pathway by
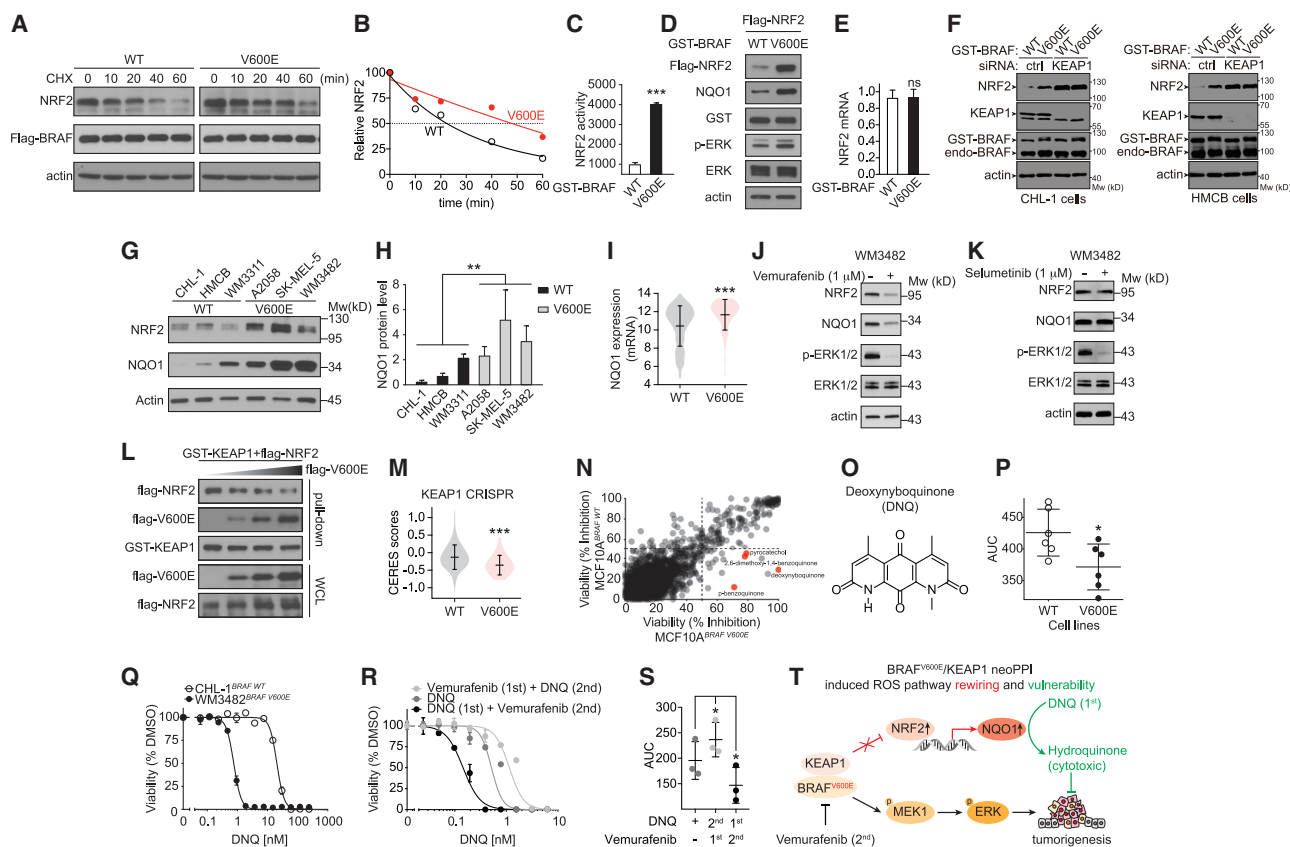
Figure 6. Neo-interaction of BRAF^{V600E} with KEAP1 and its collateral vulnerability

(A and B) BRAF^{V600E} stabilizes endogenous NRF2. Immunoblot (A) and densitometry analysis (B) showing NRF2 levels upon cycloheximide (CHX) chase in HEK293T cells overexpressing BRAF WT or V600E.

(C) BRAF^{V600E} activates NRF2 transcriptional activity. HEK293T cells were cotransfected with the NRF2-ARE luciferase reporter and either WT or V600E BRAF. Relative luciferase activity was measured, normalized to internal Renilla luciferase control. The data are presented as mean ± SD of three replicates from a representative experiment. ***$p < 0.001$.

(D) BRAF^{V600E} increases NRF2 and its target gene NQO1 protein levels in HEK293T cells transfected with GST-BRAF^{V600E} versus WT.

(E) Effect of BRAF^{V600E} on NRF2 mRNA levels in HEK293T cells transfected with flag-NRF2 and GST-BRAF WT or V600E. $^{ns}p > 0.05$.

(F) KEAP1-dependency study of BRAF^{V600E}-induced increase of NRF2 protein levels. Melanoma cells, CHL-1 (left) and HMCB (right), were transfected with KEAP1-targeting siRNA and BRAF WT or V600E plasmids as indicated. NRF2 protein expression was evaluated using western blot as indicated.

(G and H) Representative blots (G) and densitometry analysis (H) of the correlation of NRF2 and its target gene NQO1 protein levels with BRAF genetic status in six melanoma cell lines with WT or V600E BRAF. The data are presented as mean ± SD from the densitometry analysis of three representative experiments. **$p < 0.01$.

(I) Violin plot of the correlation between NQO1 mRNA levels and BRAF genetic status in 967 cell lines from CCLE dataset. The lines indicate mean ± SD. ***$p < 0.001$.

(J and K) Effect of BRAF inhibitor, vemurafenib (J), or MEK1 inhibitor, selumetinib (K), on NRF2 and NQO1 protein levels in WM3482 melanoma cell line with BRAF^{V600E} mutation.

(L) Competitive binding between BRAF^{V600E} and NRF2 to KEAP1. GST pulldown of GST-KEAP1 complex from lysate of HEK293T cells cotransfected with flag-NRF2 and with increasing amounts of flag-BRAF^{V600E}.

(M) Violin plot showing the CERES dependency scores for CRISPR knockout of KEAP1 in 342 cancer cell lines from CCLE dataset. The lines indicate mean ± SD. ***$p < 0.001$.

(N) Parallel chemogenomic screening in a pair of isogenic MCF10A cell lines. Data were presented as percentage of inhibition in parental MCF10A cells with BRAF WT versus its V600E knock in counterpart.

(O) Chemical structure of deoxynyboquinone (DNQ).

(P) AUC analysis of DNQ-induced dose-dependent growth inhibition of twelve cell lines with BRAF WT or V600E. WT: CHL-1, HMCB, MCF10A, MeWO, WM3311, and RKO$^{+/-/-}$; V600E: A2058, A375, MCF10A$^{BRAF-V600E}$, WM3482, SK-MEL-5, and RKO. Each dot represents one cell line, and the data are presented as mean ± SD. *$p < 0.05$.

(Q) Representative DNQ-induced dose-dependent growth inhibition of CHL-1 and WM3482 cell lines. The experiments were repeated independently three times. The data are presented as mean ± SEM from triplicates from a representative experiment.

(R) Sequential combination effect of DNQ and vemurafenib in growth inhibition of WM3482 cells carrying BRAF^{V600E} mutation. DNQ-induced dose-dependent growth inhibition was tested in three conditions: (1) DNQ alone, (2) pretreatment with 100 nM vemurafenib for 24 h followed by DNQ for 3 days (vemurafenib

(legend continued on next page)

directly impinging on the KEAP1-NRF2-ARE signaling axis. Indeed, overexpression of BRAF^{V600E}, but not WT, significantly stabilized NRF2 protein (Figures 6A and 6B), increased its transcriptional ARE reporter activity (Figure 6C), and increased protein levels of NRF2 and its target gene, NQO1 (NAD(P)H Quinone Dehydrogenase 1) (Figure 6D), but not NRF2 mRNA levels (Figure 6E). NRF2 protein and its downstream NQO1 protein levels (Figures 6G and 6H), but not other KEAP1 substrates including IKKβ, p62, and PGAM5 (Figure S5B), were significantly elevated in a panel of BRAF^{V600E} melanoma cell lines, as compared with that of the WT cell lines. These data were supported by the CCLE dataset, showing a positive correlation of upregulated NQO1 mRNA level with the V600E status of BRAF (Figure 6I; Table S5C). Further, treatment of BRAF^{V600E} melanoma cells with vemurafenib that decreased KEAP1 binding led to downregulated NRF2 and NQO1 protein levels (Figures 5F and 6J). The MEK1 inhibitor had no effect on the KEAP1/NRF2 activity (Figure 6K). Increased expression of BRAF^{V600E} was correlated with the reduced amount of NRF2 in the KEAP1 complex, suggesting the displacement of NRF2 from the KEAP1 complex by BRAF^{V600E} (Figure 6L). These results suggest a BRAF^{V600E}-induced KEAP1 sequestration model in which BRAF^{V600E} activates NRF2 through competitive binding with KEAP1, in addition to the previously reported transcriptional regulation mechanism (DeNicola et al., 2011). In support of this model, silencing of KEAP1 renders NRF2 protein levels unresponsive to BRAF^{V600E} status (Figure 6F). We further analyzed the CRISPR-Cas9 gene essentiality data (Meyers et al., 2017) and found that BRAF^{V600E} mutations render cancer cells dependent on KEAP1 for cell survival with increased sensitivity to KEAP1 knockout (Figure 6M; Table S5D). Thus, it is possible that BRAF^{V600E} cells might inherit intrinsic sensitivity to KEAP1-controlled pathways.

Convergence of chemical screening and BRAF^{V600E} circurty-informed therapeutic vulnerability

To search for potential therapeutic agents to exploit BRAF^{V600E}-associated vulnerability, we utilized a pair of genetically engineered MCF10A isogenic cell lines with V600E or WT of BRAF for chemical screening (Ng et al., 2018). Parallel cell viability screening with a library of bioactive compounds revealed a class of quinone compounds with selective growth inhibition of V600E cells (Figure 6N). This result corroborated the observations from the pathway analysis that connected the BRAF^{V600E}/KEAP1 interaction with enhanced activation of NQO1, a 2-electron reductase governing quinone metabolism (Dinkova-Kostova and Talalay, 2010). Thus, it is possible that the acquisition of the V600E mutation leads to elevated NQO1 function with the consequential enhanced sensitivity to toxic NQO1 substrates. To test this contention, we utilized deoxynyboquinone (DNQ) (Figure 6O), a potent and specific NQO1 substrate, to examine its effect on cell survival of BRAF^{V600E} cells (Parkinson et al.,

2013). When treated with DNQ, BRAF^{V600E}-carrying cells showed increased sensitivity over WT cells to DNQ (Figure 6P). Differential response curves were observed showing significantly enhanced sensitivity of the WM3482 cell line with BRAF^{V600E} compared with that of the CHL cell line with BRAF WT with DNQ treatment (Figure 6Q). Thus, BRAF^{V600E} in melanoma cancer cells may trigger enhanced sensitivity to NRF2-NQO1-modulated cytotoxic quinone derivatives.

Given that BRAF^{V600E}/KEAP1 neoPPI can be regulated by BRAF^{V600E} inhibitor vemurafenib (Figures 5F and 6J), we determined whether vemurafenib could synergize with DNQ in inhibiting the growth of V600E-harboring cancer cells. Using the BRAF^{V600E} mutant WM3482 cell line as a model system, treatment with vemurafenib followed by DNQ showed a slightly decrease of DNQ's potency compared with DNQ treatment alone, suggesting a negative effect of vemurafenib on DNQ (Figure 6R). However, when we reversed the order of treatment by pretreating cells with DNQ followed by vemurafenib, a significant increase of DNQ's potency was observed (Figure 6R). Such potent sequential combination effects were also observed in multiple melanoma cell lines with the BRAF^{V600E} mutation (Figure 6S). Thus, the neo-interaction of BRAF^{V600E} with KEAP1 not only rewired the NRF2 regulated redox pathway but also generated a cell state with enhanced sensitivity to cytotoxic NQO1 substrates. The uncovered BRAF^{V600E} variant-directed sequential combination strategy supports future exploration of our demonstrated neoPPIs for mechanistic investigation and neoPPI-informed therapeutic strategies (Figure 6T).

Expanded neoPPI dataset for extended oncogenic driver mutations

The extensively characterized dataset (Table S2B) supports our quantitative screening approach to identify mutation-directed neo-interactions. To provide extended resource to the scientific community, the qHT-dS approach was used to screen additional mutations of major cancer driver genes, TP53^{R282W}, PTEN^{R173C}, PTPN11^{A72V}, and EGFR^{L858R} and their WT counterparts. Through the CARINA analysis as in Figure 3A, we identified 406 SS-Df-PPIs and 253 HS-Df-PPIs (232 Go-PPI and 21 Lo-PPI) for prioritized studies (Table S6). Together, this dataset expanded the total datapoints to 2,172,864 for 17,792 PPIs tested with annotated Df-PPI candidates, providing a rich resource for cancer mutation-focused mechanistic studies.

DISCUSSION

Focusing on cancer driver mutations in this study for differential PPI discovery led to the emergence of a landscape where mutated residue-directed PPIs, and pathways may rewire oncogenic programs to shape tumor phenotypes. A suite of neoPPI candidates have been revealed that suggest alternative

---

(1st)+DNQ (2nd)), and (3) pretreatment with DNQ for 24 h followed by 100 nM vemurafenib for 3 days (DNQ(1st)+vemurafenib(2nd)). The experiments were repeated independently three times. Data are presented as mean ± SEM from triplicates from a representative experiment.

(S) AUC analysis of the combination effect of DNQ and vemurafenib in three melanoma cell lines, A2058, SK-MEL-5, and WM3482, with BRAF^{V600E} mutation. The experiments were repeated independently three times. Data are presented as mean of triplicates from a representative experiment. Each dot represents a cell line and the lines indicate mean ± SD. *p < 0.05 from paired t-test.

(T) Working model of BRAF^{V600E}/KEAP1 neoPPI in rewiring KEAP1/NRF2/NQO1 ROS pathway and generating vulnerability to NQO1 substrate.

mechanisms for well-characterized somatic aberrations. The presence of neo-interactions stemming from genomic mutations seems widespread. Also, neo-interactions were observed with different mutations in the same gene or different alterations from the same residue, emphasizing the mutated residue-driven oncogenic programs (Figures 3 and 4). Such differential connectivity of diverse mutations may be important for varying clinical phenotypes and drug sensitivity. The suggested molecular pathways mediated by these neoPPI candidates may provide opportunities to address variant-associated tumor heterogeneity and therapeutic responses.

Our results strongly support the notion that a mutated residue of an oncogenic driver may be displayed as a neo-epitope, or an induced neo-epitope, to change the composition of binding complexes. It should be noted that a protein mutation could alter its 3D structure and/or protein stability (Figure S3B), which re-wires protein-protein interactions (Sahni et al., 2015). The molecular basis for the identified neo-interactions requires structural studies of the neo-protein complexes. Functionally, such a neo-epitope(s) may drive a "partner switching" in tumor suppressor genes, leading to not only the loss of tumor suppressor function but also a gain of oncogenic potential, as shown for SPOP^{F133L} and SMAD4^{G386D} (Data S1 Figures iv–vi). Thus, unexpected widespread gain-of-interaction neoPPIs with tumor suppressor mutations may provide actionable PPI targets for therapeutic intervention. Both Go-PPIs and Lo-PPIs identified may be targeted for therapeutic development through the discovery of neoPPI inhibitors or hypomorph-PPI inducers (Tang et al., 2021).

The uncovered oncogenic mutation-mediated neoPPI candidates suggest mechanistic hypothesis to address observed clinical phenotypes of defined alterations. For example, the BRAF^{V600E}/KEAP1 interaction informs potential ROS homeostasis pathway reprogramming (Data S1 Figure ii). However, such mechanistic interpretations require in-depth neoPPI characterization and functional analysis. It is critical to verify the identified neoPPIs in relevant cancer types under the endogenous conditions to mitigate overexpression and tag-associated artifacts (Figure 4). We presented the BRAF^{V600E}/KEAP1 interaction as a case study to advance our neoPPI candidate based on extensive interaction data including direct binding and those from BRAF^{V600E}-carrying patient-derived cancer cells. The dynamic interaction complex among BRAF^{V600E}, KEAP1, and NRF2 demonstrates a potential mechanism by which BRAF^{V600E} contributes to tumorigenesis and presents a promising molecular target for therapeutic intervention (Figure 6T) (Hintsala et al., 2016; Shirazi et al., 2020). The BRAF^{V600E}/KEAP1 neoPPI-rewired pathway also exposes a potential vulnerability, leading to a sequential combination strategy for patients with BRAF^{V600E}. Such therapeutic insights informed by the discovered BRAF^{V600E}/KEAP1 neoPPI exemplifies the utility of neoPPIs as a starting point to reveal hidden pathway dependencies and vulnerabilities.

The recurrent neoPPI binding partners converge onto demonstrated core oncogenic pathways, including the cancer intrinsic JAK-STAT immune response pathway (Zaretsky et al., 2016), providing a molecular basis for the oncogenic function of various driver mutations. On the other hand, driver mutations also generate distinct neoPPIs that may lead to divergent pathway rewiring, offering targets for precision therapy.

Our systematic discovery of mutant-induced neoPPI candidates is enabled by the qHT-dS platform that permits the identification of Df-PPIs at single amino acid resolution. This PPI detection approach emphasizes the quality of the PPI data from CARINA analysis of binary titration and quadruplicate samples and the quantitative nature for cancer-focused differential PPI mapping in physiologically relevant environment, complementing the computational, AP-MS, and Y2H technologies for proteome scale studies (Cheng et al., 2021; Do et al., 2012; Sahni et al., 2015). In comparison to human interactome datasets, such as BioGRID and BioPlex v2 (Oughtred et al., 2019; Rolland et al., 2014), the qHT-dS PPI profiling has also significantly expanded the connectivity within the OncoPPI space.

Together, our results support the concept of mutation-driven oncogenic pathway rewiring through mutant-allele-enabled PPIs. The experimentally validated neoPPI candidates provide a mechanistic basis to generate testable hypothesis to further examine their functional significance. Such mutation-dictated PPIs may not only enhance our understanding of molecular reprograming in cancer but also reveal potential ways to target tumor variant-mediated mechanisms for therapeutic intervention, which may be applicable to genomic alterations in both oncogenes and tumor suppressors. The presented Df-PPI dataset and the neoPPI candidates from our quantitative screening platform, bioinformatics and experimental annotation, and confirmative studies offer the scientific community a valuable resource for variant-directed molecular interaction studies to accelerate the precision medicine approach.

Limitations of the study

The qHT-dS platform leverages a live cell-based BRET biosensor with tags and the protein overexpression system, and thus, the stoichiometry achieved in the qHT-dS system could be different from the actual situation in relevant cells. To mitigate potential caveat of nonspecific interactions, the use of Df-PPI dataset requires orthogonal PPI and functional analysis with alternative readouts and tag-free assays in physiologically relevant cellular systems to advance neoPPIs (Figure 4). Such studies require high-quality antibodies for detecting endogenous partners and co-IP under native states. The 3D structural analysis of neo-protein complexes will be important to reveal the mode of interactions to determine whether the mutated residues directly mediate neoPPIs. The current studies focused on cancer-associated mutations and genes, whereas the majority of protein-coding genes in the genome is not assessed. Our promising results support the expansion of the study to the proteome scale and to other disease-associated mutations.

STAR★METHODS

Detailed methods are provided in the online version of this paper and include the following:

- KEY RESOURCES TABLE
- RESOURCE AVAILABILITY
  ○ Lead contact
  ○ Materials availability
  ○ Data and code availability

Cell
Resource

- ● EXPERIMENTAL MODEL AND SUBJECT DETAILS
- ● METHOD DETAILS
  - ○ OncoPPI v2 library of cancer-associated genes
  - ○ qHT-dS platform for Df-PPI screening
  - ○ CARINA algorithm for data analysis and statistics
  - ○ Gene pathway enrichment analysis
  - ○ Molecular biology techniques and cell culture conditions
  - ○ Nanoluc protein-fragment complementation assay (NanoPCA)
  - ○ GST pulldown, flag-immunoprecipitation and co-immunoprecipitation (co-IP) assays
  - ○ Venus Protein-fragment Complementation Assay (PCA)
  - ○ BioLayer Interferometry (BLI)
  - ○ RNA isolation, cDNA synthesis and qPCR
  - ○ Protein stability assays
  - ○ Luciferase reporter assay
  - ○ HTS cell viability assay
- ● QUANTIFICATION AND STATISTICAL ANALYSIS

SUPPLEMENTAL INFORMATION

Supplemental information can be found online at https://doi.org/10.1016/j.cell.2022.04.014.

AUTHOR CONTRIBUTIONS

X.M., Q.N., A.A.I., Y.T.H., C.T., X.Y., C.S., S.D., D.C., D.F., Q.L., K.Q., and Y.D. conducted the experiments; X.M., Q.N., A.A.I., A.W., M.A.R., L.A.D.C., C.S.M., W.Z., T.O., S.L., F.R.K., Y.D., S.S.R., G.D.M., and H.F. participated in data analysis and interpretation; X.M., Q.N., A.A.I., G.B.M., F.R.K., Y.D., and H.F. participated in discussion and manuscript preparation; X.M., Q.N., A.A.I., D.C., Y.D., and H.F. designed the experiments and wrote the paper; and all were involved in manuscript editing.

REFERENCES

Arkin, M.R., Tang, Y., and Wells, J.A. (2014). Small-molecule inhibitors of protein-protein interactions: progressing toward the reality. Chem. Biol. *21*, 1102–1114.

Boehme, K.A., Kulikov, R., and Blattner, C. (2008). p53 stabilization in response to DNA damage requires Akt/PKB and DNA-PK. Proc. Natl. Acad. Sci. USA *105*, 7785–7790.

Burd, C.E., Liu, W., Huynh, M.V., Waqas, M.A., Gillahan, J.E., Clark, K.S., Fu, K., Martin, B.L., Jeck, W.R., Souroullas, G.P., et al. (2014). Mutation-specific RAS oncogenicity explains NRAS codon 61 selection in melanoma. Cancer Discov. *4*, 1418–1429.

Cancer Genome Atlas Research Network, Weinstein, J.N., Collisson, E.A., Mills, G.B., Shaw, K.R., Ozenberger, B.A., Ellrott, K., Shmulevich, I., Sander, C., and Stuart, J.M. (2013). The Cancer Genome Atlas Pan-Cancer analysis project. Nat. Genet. *45*, 1113–1120.

Cancer Target Discovery and Development Network, Schreiber, S.L., Shamji, A.F., Clemons, P.A., Hon, C., Koehler, A.N., Munoz, B., Palmer, M., Stern, A.M., Wagner, B.K., et al. (2010). Towards patient-based cancer therapeutics. Nat. Biotechnol. *28*, 904–906.

Carpten, J.D., Faber, A.L., Horn, C., Donoho, G.P., Briggs, S.L., Robbins, C.M., Hostetter, G., Boguslawski, S., Moses, T.Y., Savage, S., et al. (2007). A transforming mutation in the pleckstrin homology domain of AKT1 in cancer. Nature *448*, 439–444.

Ceccaldi, R., Sarangi, P., and D'Andrea, A.D. (2016). The Fanconi anaemia pathway: new players and new functions. Nat. Rev. Mol. Cell Biol. *17*, 337–349.

Chang, M.T., Asthana, S., Gao, S.P., Lee, B.H., Chapman, J.S., Kandoth, C., Gao, J., Socci, N.D., Solit, D.B., Olshen, A.B., et al. (2016). Identifying recurrent mutations in cancer reveals widespread lineage diversity and mutational specificity. Nat. Biotechnol. *34*, 155–163.

Chen, Y., Huang, L., Dong, Y., Tao, C., Zhang, R., Shao, H., and Shen, H. (2020). Effect of AKT1 (p. E17K) Hotspot Mutation on Malignant Tumorigenesis and Prognosis. Front. Cell Dev. Biol. *8*, 573599.

Cheng, F., Zhao, J., Wang, Y., Lu, W., Liu, Z., Zhou, Y., Martin, W.R., Wang, R., Huang, J., Hao, T., et al. (2021). Comprehensive characterization of protein-protein interactions perturbed by disease mutations. Nat. Genet. *53*, 342–353.

Ciriello, G., Cerami, E., Sander, C., and Schultz, N. (2012). Mutual exclusivity analysis identifies oncogenic network modules. Genome Res. *22*, 398–406.

DeNicola, G.M., Karreth, F.A., Humpton, T.J., Gopinathan, A., Wei, C., Frese, K., Mangal, D., Yu, K.H., Yeo, C.J., Calhoun, E.S., et al. (2011). Oncogene-induced Nrf2 transcription promotes ROS detoxification and tumorigenesis. Nature *475*, 106–109.

Dinkova-Kostova, A.T., and Talalay, P. (2010). NAD(P)H:quinone acceptor oxidoreductase 1 (NQO1), a multifunctional antioxidant enzyme and exceptionally versatile cytoprotector. Arch. Biochem. Biophys. *501*, 116–123.

Do, P.M., Varanasi, L., Fan, S., Li, C., Kubacka, I., Newman, V., Chauhan, K., Daniels, S.R., Boccetta, M., Garrett, M.R., et al. (2012). Mutant p53 cooperates with ETS2 to promote etoposide resistance. Genes Dev. *26*, 830–845.

Forbes, S.A., Beare, D., Boutselakis, H., Bamford, S., Bindal, N., Tate, J., Cole, C.G., Ward, S., Dawson, E., Ponting, L., et al. (2017). COSMIC: somatic cancer genetics at high-resolution. Nucleic Acids Res. *45*, D777–D783.

Frampton, G.M., Fichtenholtz, A., Otto, G.A., Wang, K., Downing, S.R., He, J., Schnall-Levin, M., White, J., Sanford, E.M., An, P., et al. (2013). Development and validation of a clinical cancer genomic profiling test based on massively parallel DNA sequencing. Nat. Biotechnol. *31*, 1023–1031.

Garcia-Higuera, I., Taniguchi, T., Ganesan, S., Meyn, M.S., Timmers, C., Hejna, J., Grompe, M., and D'Andrea, A.D. (2001). Interaction of the fanconi anemia proteins and BRCA1 in a common pathway. Mol. Cell *7*, 249–262.

Hahn, W.C., Bader, J.S., Braun, T.P., Califano, A., Clemons, P.A., Druker, B.J., Ewald, A.J., Fu, H., Jagu, S., Kemp, C.J., et al. (2021). An expanded universe of cancer targets. Cell *184*, 1142–1155.

Haling, J.R., Sudhamsu, J., Yen, I., Sideris, S., Sandoval, W., Phung, W., Bravo, B.J., Giannetti, A.M., Peck, A., Masselot, A., et al. (2014). Structure of the BRAF-MEK complex reveals a kinase activity independent role for BRAF in MAPK signaling. Cancer Cell *26*, 402–413.

Hintsala, H.R., Jokinen, E., Haapasaari, K.M., Moza, M., Ristimäki, A., Soini, Y., Koivunen, J., and Karihtala, P. (2016). Nrf2/Keap1 Pathway and Expression

of Oxidative Stress Lesions 8-hydroxy-2′-deoxyguanosine and Nitrotyrosine in Melanoma. Anticancer Res. 36, 1497–1506.

Ivanov, A.A., Khuri, F.R., and Fu, H. (2013). Targeting protein-protein interactions as an anticancer strategy. Trends Pharmacol. Sci. 34, 393–400.

Jaramillo, M.C., and Zhang, D.D. (2013). The emerging role of the Nrf2-Keap1 signaling pathway in cancer. Genes Dev. 27, 2179–2191.

Kamburov, A., Lawrence, M.S., Polak, P., Leshchiner, I., Lage, K., Golub, T.R., Lander, E.S., and Getz, G. (2015). Comprehensive assessment of cancer missense mutation clustering in protein structures. Proc. Natl. Acad. Sci. U. S. A. 112, E5486–E5495.

Kandel, E.S., Skeen, J., Majewski, N., Di Cristofano, A., Pandolfi, P.P., Feliciano, C.S., Gartel, A., and Hay, N. (2002). Activation of Akt/protein kinase B overcomes a G(2)/m cell cycle checkpoint induced by DNA damage. Mol. Cell. Biol. 22, 7831–7841.

Karoulia, Z., Gavathiotis, E., and Poulikakos, P.I. (2017). New perspectives for targeting RAF kinase in human cancer. Nat. Rev. Cancer 17, 676–691.

Lawrence, M.S., Stojanov, P., Mermel, C.H., Robinson, J.T., Garraway, L.A., Golub, T.R., Meyerson, M., Gabriel, S.B., Lander, E.S., and Getz, G. (2014). Discovery and saturation analysis of cancer genes across 21 tumour types. Nature 505, 495–501.

Li, Z., Ivanov, A.A., Su, R., Gonzalez-Pecchi, V., Qi, Q., Liu, S., Webber, P., McMillan, E., Rusnak, L., Pham, C., et al. (2017). The OncoPPi network of cancer-focused protein-protein interactions to inform biological insights and therapeutic strategies. Nat. Commun. 8, 14356.

Martínez-Jiménez, F., Muiños, F., Sentís, I., Deu-Pons, J., Reyes-Salazar, I., Arnedo-Pac, C., Mularoni, L., Pich, O., Bonet, J., Kranas, H., et al. (2020). A compendium of mutational cancer driver genes. Nat. Rev. Cancer 20, 555–572.

Matsuoka, S., Ballif, B.A., Smogorzewska, A., McDonald, E.R., 3rd, Hurov, K.E., Luo, J., Bakalarski, C.E., Zhao, Z., Solimini, N., Lerenthal, Y., et al. (2007). ATM and ATR substrate analysis reveals extensive protein networks responsive to DNA damage. Science 316, 1160–1166.

Menzies, A.M., Haydu, L.E., Visintin, L., Carlino, M.S., Howle, J.R., Thompson, J.F., Kefford, R.F., Scolyer, R.A., and Long, G.V. (2012). Distinguishing clinico-pathologic features of patients with V600E and V600K BRAF-mutant metastatic melanoma. Clin. Cancer Res. 18, 3242–3249.

Meyers, R.M., Bryan, J.G., McFarland, J.M., Weir, B.A., Sizemore, A.E., Xu, H., Dharia, N.V., Montgomery, P.G., Cowley, G.S., Pantel, S., et al. (2017). Computational correction of copy number effect improves specificity of CRISPR-Cas9 essentiality screens in cancer cells. Nat. Genet. 49, 1779–1784.

Mo, X., Qi, Q., Ivanov, A.A., Niu, Q., Luo, Y., Havel, J., Goetze, R., Bell, S., Moreno, C.S., Cooper, L.A., et al. (2017). AKT1, LKB1, and YAP1 revealed as MYC interactors with NanoLuc-based protein-fragment complementation assay. Mol. Pharmacol. 91, 339–347.

Mo, X.L., and Fu, H. (2016). BRET: NanoLuc-based bioluminescence resonance energy transfer platform to monitor protein-protein interactions in live cells. Methods Mol. Biol. 1439, 263–271.

Mo, X.L., Luo, Y., Ivanov, A.A., Su, R., Havel, J.J., Li, Z., Khuri, F.R., Du, Y., and Fu, H. (2016). Enabling systematic interrogation of protein-protein interactions in live cells with a versatile ultra-high-throughput biosensor platform. J. Mol. Cell Biol. 8, 271–281.

Ng, P.K., Li, J., Jeong, K.J., Shao, S., Chen, H., Tsang, Y.H., SenGupta, S., Wang, Z., Bhavana, V.H., Tran, R., et al. (2018). Systematic functional annotation of somatic mutations in cancer. Cancer Cell 33, 450–462.e10.

Oughtred, R., Stark, C., Breitkreutz, B.J., Rust, J., Boucher, L., Chang, C., Kolas, N., O'Donnell, L., Leung, G., McAdam, R., et al. (2019). The BioGRID interaction database: 2019 update. Nucleic Acids Res. 47, D529–D541.

Parkinson, E.I., Bair, J.S., Cismesia, M., and Hergenrother, P.J. (2013). Efficient NQO1 substrates are potent and selective anticancer agents. ACS Chem. Biol. 8, 2173–2183.

Pham, C.D. (2015). Detection of protein-protein interaction using bimolecular fluorescence complementation assay. Methods Mol. Biol. 1278, 483–495.

Rolland, T., Taşan, M., Charloteaux, B., Pevzner, S.J., Zhong, Q., Sahni, N., Yi, S., Lemmens, I., Fontanillo, C., Mosca, R., et al. (2014). A proteome-scale map of the human interactome network. Cell 159, 1212–1226.

Sahni, N., Yi, S., Taipale, M., Fuxman Bass, J.I., Coulombe-Huntington, J., Yang, F., Peng, J., Weile, J., Karras, G.I., Wang, Y., et al. (2015). Widespread macromolecular interaction perturbations in human genetic disorders. Cell 161, 647–660.

Shiloh, Y., and Ziv, Y. (2013). The ATM protein kinase: regulating the cellular response to genotoxic stress, and more. Nat. Rev. Mol. Cell Biol. 14, 197–210.

Shirazi, F., Jones, R.J., Singh, R.K., Zou, J., Kuiatse, I., Berkova, Z., Wang, H., Lee, H.C., Hong, S., Dick, L., et al. (2020). Activating KRAS, NRAS, and BRAF mutants enhance proteasome capacity and reduce endoplasmic reticulum stress in multiple myeloma. Proc. Natl. Acad. Sci. USA 117, 20004–20014.

Sporn, M.B., and Liby, K.T. (2012). NRF2 and cancer: the good, the bad and the importance of context. Nat. Rev. Cancer 12, 564–571.

Tang, C., Mo, X., Niu, Q., Wahafu, A., Yang, X., Qui, M., Ivanov, A.A., Du, Y., and Fu, H. (2021). Hypomorph mutation-directed small-molecule protein-protein interaction inducers to restore mutant SMAD4-suppressed TGF-beta signaling. Cell Chem. Biol. 28, 636–647.e5.

Viniegra, J.G., Martínez, N., Modirassari, P., Hernández Losa, J., Parada Cobo, C., Sánchez-Arévalo Lobo, V.J., Aceves Luquero, C.I., Alvarez-Vallina, L., Ramón y Cajal, S., Rojas, J.M., et al. (2005). Full activation of PKB/Akt in response to insulin or ionizing radiation is mediated through ATM. J. Biol. Chem. 280, 4029–4036.

Vivanco, I., Robins, H.I., Rohle, D., Campos, C., Grommes, C., Nghiemphu, P.L., Kubek, S., Oldrini, B., Chheda, M.G., Yannuzzi, N., et al. (2012). Differential sensitivity of glioma- versus lung cancer-specific EGFR mutations to EGFR kinase inhibitors. Cancer Discov. 2, 458–471.

Vogelstein, B., Papadopoulos, N., Velculescu, V.E., Zhou, S., Diaz, L.A., Jr., and Kinzler, K.W. (2013). Cancer genome landscapes. Science 339, 1546–1558.

Westcott, P.M., Halliwill, K.D., To, M.D., Rashid, M., Rust, A.G., Keane, T.M., Delrosario, R., Jen, K.Y., Gurley, K.E., Kemp, C.J., et al. (2015). The mutational landscapes of genetic and chemical models of Kras-driven lung cancer. Nature 517, 489–492.

Xie, Z., Bailey, A., Kuleshov, M.V., Clarke, D.J.B., Evangelista, J.E., Jenkins, S.L., Lachmann, A., Wojciechowicz, M.L., Kropiwnicki, E., Jagodnik, K.M., et al. (2021). Gene set knowledge discovery with Enrichr. Curr. Protoc. 1, e90.

Zaretsky, J.M., Garcia-Diaz, A., Shin, D.S., Escuin-Ordinas, H., Hugo, W., Hu-Lieskovan, S., Torrejon, D.Y., Abril-Rodriguez, G., Sandoval, S., Barthly, L., et al. (2016). Mutations associated with acquired resistance to PD-1 blockade in melanoma. N. Engl. J. Med. 375, 819–829.

Cell
Resource

🔗 CellPress

STAR★METHODS

KEY RESOURCES TABLE

REAGENT or RESOURCE	SOURCE	IDENTIFIER
Antibodies		
Mouse monoclonal anti-FLAG-HRP antibody	Sigma-Aldrich	Cat# A8592; RRID: AB_439702
Rabbit polyclonal anti-GST-HRP antibody	Sigma-Aldrich	Cat# A7340; RRID: AB_258340
Mouse monoclonal anti-β-Actin antibody	Sigma-Aldrich	Cat# A5441; RRID: AB_476744
Mouse monoclonal anti-BRAF	Santa Cruz	Cat# sc-5284; RRID:AB_2721130
Rabbit polyclonal anti-NRF2 antibody	Abcam	Cat# ab62352; RRID:AB_944418
Mouse monoclonal anti-NQO1 antibody	Santa Cruz	Cat# sc-32793; RRID:AB_628036
Rabbit polyclonal anti-KEAP1 antibody	Cell Signaling	Cat# 4678; RRID:AB_10548196
Rabbit polyclonal anti-KEAP1 antibody	Proteintech	Cat# 10503-2-AP; RRID:AB_2132625
Rabbit polyclonal anti-CUL3 antibody	Cell Signaling	Cat# 2759; RRID:AB_2086432
Rabbit monoclonal anti-ERBB3 antibody	Cell Signaling	Cat# 12708; RRID:AB_2721919
Rabbit monoclonal anti-GNA13 antibody	Abcam	Cat# ab128900; RRID:AB_11142234
Rabbit monoclonal anti-GSK3β antibody	Cell Signaling	Cat# 9315; RRID:AB_490890
Rabbit monoclonal anti-HDAC1 antibody	Cell Signaling	Cat# 34589; RRID:AB_2756821
Rabbit monoclonal anti-LATS1 antibody	Cell Signaling	Cat# 3477; RRID:AB_2133513
Rabbit monoclonal anti-NOTCH2 antibody	Cell Signaling	Cat#5732; RRID:AB_10693319
Rabbit polyclonal anti-POLD1 antibody	Proteintech	Cat# 15646-1-AP; RRID:AB_2252572
Rabbit monoclonal anti-SDHB antibody	Cell Signaling	Cat# 92649
Rabbit polyclonal anti-SMAD1 antibody	Cell Signaling	Cat# 9743; RRID:AB_2107780
Rabbit polyclonal anti-ASXL2 antibody	Bethyl Laboratories	Cat# A302-037A; RRID:AB_1576481
Rabbit monoclonal anti-c-JUN antibody	Cell Signaling	Cat#9165; RRID:AB_2130165
Rabbit polyclonal anti-CUL4B antibody	Proteintech	Cat#12916-1-AP
Rabbit polyclonal anti-ZBTB2 antibody	Bethyl Laboratories	Cat# A303-262; RRID:AB_10952231
Rabbit monoclonal anti-ATM antibody	Cell Signaling	Cat# 2873; RRID:AB_2062659
Rabbit polyclonal anti-STAG2 antibody	Cell Signaling	Cat# 5882; RRID:AB_10834529
Rabbit polyclonal anti-p38-delta (MAPK13) antibody	Cell Signaling	Cat# 2308; RRID:AB_10694398
Rabbit monoclonal anti-beta-arrestin2 (ARRB2) antibody	Cell Signaling	Cat# 3857; RRID:AB_2258681
Rabbit monoclonal anti-SKP2 antibody	Cell Signaling	Cat# 2652; RRID:AB_11178941
Rabbit anti-mTOR antibody	Cell Signaling	Cat# 2972; RRID:AB_330978
Rabbit polyclonal anti-NPM1 antibody	Cell Signaling	Cat# 3542; RRID:AB_2155178
Rabbit polyclonal anti-RPS2 antibody	Bethyl Laboratories	Cat# A303-794A-M; RRID:AB_2781471
Rabbit polyclonal anti-STARD3 antibody	Invitrogen	Cat# PA1-562; RRID:AB_2197799
Rabbit monoclonal anti-BTG1 antibody	Abcam	Cat# ab151740
Rabbit polyclonal anti-VHL antibody	Cell signaling	Cat# 68547; RRID:AB_2716279
Rabbit monoclonal anti-BCL-xL (BCL2L1) antibody	ThermoFisher	Cat# MA5-15142; RRID:AB_10979212
Rabbit polyclonal anti-GOT1 antibody	Proteintech	Cat# 14886-1-AP; RRID:AB_2113630
Rabbit polyclonal anti-PDCD2L antibody	Bethyl Laboratories	Cat# A303-783A; RRID:AB_11218393
Rabbit monoclonal anti-AURKA antibody	Cell signaling	Cat# 14475; RRID:AB_2665504
Rabbit monoclonal anti-GSK3A antibody	Cell signaling	Cat# 4337; RRID:AB_10859910
Rabbit monoclonal anti-SUFU antibody	Cell signaling	Cat# 2522; RRID:AB_2302728
Rabbit polyclonal anti-MAPK7 antibody	Proteintech	Cat# 11164-1-AP; RRID:AB_2877749

(Continued on next page)

Continued

REAGENT or RESOURCE	SOURCE	IDENTIFIER
Rabbit polyclonal anti-Menin (MEN1) antibody	ThermoFisher	Cat# PA5-79663; RRID:AB_2746778
Rabbit monoclonal anti-FOXO3a antibody	Cell signaling	Cat# 2497; RRID:AB_836876
Rabbit monoclonal anti-IKK-beta (IKBKB) antibody	Cell signaling	Cat# 8943; RRID:AB_11024092
Rabbit monoclonal anti-MAPK6 antibody	Abcam	Cat# ab53277; RRID:AB_2140288
Rabbit polyclonal anti-ITPKB antibody	Proteintech	Cat# 12816-1-AP; RRID:AB_2129846
Rabbit polyclonal anti-POLE antibody	GeneTex	Cat# GTX132100; RRID:AB_2886567
Mouse Anti-Rabbit IgG (Light-Chain Specific) (D4W3E) mAb (HRP Conjugate)	Cell signaling	Cat# 93702; RRID: AB_2800208
Rabbit polyclonal anti- p44/42 MAPK (Erk1/2) antibody	Cell signaling	Cat# 9102; RRID:AB_330744
Rabbit monoclonal anti-phospho-p44/42 MAPK (Erk1/2) (Thr202/Tyr204) antibody	Cell signaling	Cat# 4370; RRID:AB_2315112
Rabbit polyclonal anti-histone H2A.X antibody	Cell signaling	Cat# 2595; RRID:AB_10694556
Rabbit polyclonal phospho-Histone H2A.X (Ser139) Antibody	Cell signaling	Cat# 2577; RRID:AB_2118010
Rabbit monoclonal anti-Ferritin antibody	Abcam	Cat# ab75973; RRID:AB_1310222
Peroxidase AffiniPure Goat Anti-Rabbit IgG(H+L) secondary antibody	Jackson ImmunoResearch	Cat# 111-035-003; RRID:AB_2313567
Peroxidase AffiniPure Goat Anti-Mouse IgG(H+L) secondary antibody	Jackson ImmunoResearch	Cat# 115-035-003; RRID:AB_10015289
Bacterial and virus strains		
One Shot TOP10 Chemically Competent E. coli cells	ThermoFisher Scientific	Cat# C404010
XL10-Gold ultracompetent cells	Agilent	Cat# 200315
Chemicals, peptides, and recombinant proteins		
Emory Enriched Bioactive Chemical library	Emory ECBDC; PMID: 30639259; 33326750	N/A
deferoxamine mesylate (DFOM)	Selleckchem	Cat# S5742; CAS No. 1032-65-1
Vemurafenib	Selleckchem	Cat# S1267; CAS No. 918504-65-1
Selumetinib	Selleckchem	Cat# S1008; CAS No. 606143-52-6
Cycloheximide	Selleckchem	Cat# S7418; CAS No. 66-81-9
Deoxynyboquinone (DNQ)	Gift from Dr. Paul J. Hergenrother; PMID: 23937670	CAS No. 96748-86-6
Recombinant human GST-tag BRAF-WT protein	Abcam	Cat# ab204208
Recombinant human GST-tag BRAF-V600E protein	Abcam	Cat# ab204154
Critical commercial assays		
CellTiter-Blue® Cell Viability Assay	Promega	Cat# G8081
Dual-Glo® Luciferase Assay System	Promega	Cat# E2920
Deposited data		
Raw and analyzed protein-protein interaction screening data	This paper (Table 3-4; 13-14)	https://ocg.cancer.gov/programs/ctd2/data-portal
Experimental models: Cell lines		
HEK293T cell line	ATCC	Cat# CRL-3216; RRID: CVCL_0063
A375 cell line	ATCC	Cat# CRL-1619; RRID:CVCL_0132
HMCB cell line	ATCC	Cat# CRL-9607; RRID:CVCL_3317

(Continued on next page)

Cell
Resource

Continued

REAGENT or RESOURCE	SOURCE	IDENTIFIER
CHL-1 cell line	ATCC	Cat# CRL-9446; RRID:CVCL_1122
WM3311 cell line	Rockland Immunochemicals Inc.	Cat# WM3311-01-0001
WM3482 cell line	Rockland Immunochemicals Inc.	Cat# WM3482-01-0001
A2058 cell line	ATCC	Cat# CRL-11147; RRID:CVCL_1059
SK-MEL-5 cell line	ATCC	Cat# HTB-70; RRID:CVCL_0527
LOXIMVI cell line	Millipore	Cat# SCC201; RRID:CVCL_1381
RPMI-7951 cell line	ATCC	Cat# HTB-66; RRID:CVCL_1666
SK-MEL-28 cell line	ATCC	Cat# HTB-72; RRID:CVCL_0526
UACC257 (U257) cell line	NCI-DTP	Cat# UACC-257; RRID:CVCL_1779
WM88 cell line	Rockland Immunochemicals Inc.	Cat# WM88-01-0001; RRID:CVCL_6805
CJM cell line	Gift from Dr. Stuart Scheiber; PMID: 28678785	RRID: CVCL_U797
Parental MCF10A cell line	Horizon Discovery	Cat# HD PAR-003; RRID:CVCL_0598
Isogenic MCF10A BRAF V600E cell line	Horizon Discovery	Cat# HD 101-012
Parental RKO cells (+/V600E/V600E) cell line	Horizon Discovery	Cat# HD PAR-007; RRID:CVCL_0504
Isogenic RKO BRAF (+/-/-)cell line	Horizon Discovery	Cat# HD 106-003
MCF7 cell line	ATCC	Cat# HTB-22; RRID:CVCL_0031
Isogenic MCF7 AKT1 WT cell line	Gift from Dr. Josh Lauring; PMID: 23888070	N/A
Isogenic MCF7 AKT1 E17K cell line	Gift from Dr. Josh Lauring; PMID: 23888070	N/A
NCI-H1299 cell line	ATCC	Cat# CRL-5803; RRID:CVCL_0060
HCT116 cell line	ATCC	Cat# CCL-247; RRID: CVCL_0291
C4-2 cell line	ATCC	Cat# CRL-3314; RRID:CVCL_4782
Oligonucleotides		
qPCR primers for NRF2: Forward: GCGAC GGAAAGAGTATGAGC; Reverse: GTTGGC AGATCCACTGGTTT	IDT	N/A
qPCR primers for GAPDH: Forward: ATGT TCGTCATGGGTGTGAA; Reverse: AGTT GTCATGGATGACCTTGG	IDT	N/A
ON-TARGETplus Human KEAP1 siRNA	Horizon Discovery	Cat# is L-012453-00-0010
Recombinant DNA		
OncoPPi v2 library	This paper	N/A
OncoMut library	This paper	N/A
TCF/LEF transcriptional luciferase reporter plasmid	BPS Bioscience	Cat# 60500
AP-1 transcriptional luciferase reporter plasmid	Qiagen	Cat# CCS-011L
NRF2-ARE luciferase reporter plasmid	BPS Bioscience	Cat# 60514
pET15b-KEAP1-KELCH plasmid	Gift from Dr. Donna Zhang; PMID: 15475350	N/A
Software and algorithms		
Graphpad	Graphpad; v7	https://www.graphpad.com/scientific-software/prism/
Cytoscape	Cytoscape; v3.9.0	https://cytoscape.org
Matlab	Mathworks	https://www.mathworks.com/products/get-matlab.html
CARINA	This paper	N/A
Python	Python	https://www.python.org
Schrödinger software	Schrödinger	https://www.schrodinger.com

Cell
Resource

RESOURCE AVAILABILITY

Lead contact
Further information and requests for resources and reagents should be directed to and will be fulfilled by the lead contact, Haian Fu (hfu@emory.edu).

Materials availability
Plasmids generated in this study are available upon request to the Lead contact. Other materials are available through commercial sources (see Key Resource Table).

Data and code availability
PPI screening datasets are available through CTD^2 data portal (https://ocg.cancer.gov/programs/ctd2/data-portal).

All original code reported in this paper is available from lead contact upon request.

Additional information required to reanalyze the data reported in this paper is available from lead contact upon request.

EXPERIMENTAL MODEL AND SUBJECT DETAILS

All cells were incubated at 37°C in humidified conditions with 5% CO_2. Human cancer cell lines (CHL-1, HMCB, A2058, and SK-MEL-5 from ATCC, Manassas, VA; WM3311, and WM3482 from Rockland Immunochemicals Inc., Limerick, PA; parental MCF10A, isogenic BRAF^{V600E} knockin MCF10A, parental RKO, and isogenic BRAF V600E mutant alleles knockout RKO, and engineered RKO with flag-tag knockin from Horizon Discovery (Saint Louis, MO) were cultured in cell culture media suggested by manufacturer. HEK293T cells (ATCC, Manassas, VA) were maintained in regular Dulbecco's Modified Eagle's Medium (DMEM, Corning, 10013CV), supplemented with 10% fetal bovine serum (FBS, Sigma, F0926) and 1x penicillin/streptomycin solution (Corning, 3001Cl), or in phenol red free DMEM (HyClone, SH30284.01) throughout the screening. For drug treatment for functional studies, cells were treated with either vehicle or chemicals at indicated concentration.

METHOD DETAILS

OncoPPI v2 library of cancer-associated genes
Genes collected for the current studies are listed in Table S1. The OncoPPi v2 library includes all genes from the OncoPPi v1 gene set of lung cancer associated genes (Li et al., 2017). To expand the OncoPPi library to other cancer types, we have identified the major tumor driver and tumor suppressor genes determined in large-scale cancer genomics studies (Cancer Genome Atlas Research et al., 2013; Forbes et al., 2017; Frampton et al., 2013; Lawrence et al., 2014), such as The Cancer Genome Atlas (TCGA) (https://www.cancer.gov/tcga). Based on the analysis of cancer-associated pathways defined in MSigDB, Reactome, and KEGG databases, we also included proteins involved in the regulation of oncogenic programs. Genes were selected based on their association with tumor pathogenesis in cancer patients (Figure S2A; Table S1). The library is significantly enriched in different oncogenic pathways (e.g., p= 2.64e-94), cancer hallmarks (Figure S2B), and defined oncogenes and tumor suppressors (Figure S2C). These genes were cloned, sequence-verified, and used to create a collection of mammalian expression vectors with biosensor tags for 556 distinct human WT protein-coding ORFs (Table S1). All genes included in OncoPPi v2 library were annotated with the frequency of genomic alterations observed in the TCGA PanCancer patient cohorts available through the NCI Genomics Data Commons (GDC) Portal.

Each gene was subcloned into the indicated Gateway entry vector (Invitrogen). The integrity of the genes was confirmed by BsrGI restriction digestion and sequencing, generating the entry-vector library. Genes in the entry vector library were transferred using the Gateway recombination system to the destination expression vector to produce a Venus-flag-gene fusion for each gene, generating the OncoPPi v2 expression vector library. Site-directed mutagenesis was used to generate cancer driver mutation entry-vectors, which were fully sequenced and then transferred using Gateway recombination system to destination expression vector to produce a NLuc-HA-gene fusion for each cancer driver MUT and WT.

qHT-dS platform for Df-PPI screening
We used our previously established BRET^n technology in miniaturized uHTS 1536-well plate-based format to develop a qHT-dS platform to assess PPIs in live-cells for parallel comparative screening. NLuc- and Venus-fusion proteins allow streamlined monitoring of protein expressions simultaneously with BRET signal detection in a simple add-and-read mode. Briefly, HEK293T cells (1500 cells in 4 μl per well) were cultured in 1536-well plates at 37 $^{\circ}$C before they were co-transfected in wells with Venus-tagged genes in combination with NLuc-tagged genes using Linear polyethylenimines (PEIs, Polysciences, 23966). Transfection was performed by adding 1 μl mixture of PEI (30 ng/μl) and DNA (10 ng/μl) to 4 μl cell culture, assisted by robotic operations with the Biomek NX^P Lab Automation Workstation (Beckman Coulter). BRET saturation assay was performed by titration of DNA amount to achieve various NLuc- and Venus-tagged gene combinations.

After incubation for 48 hours, Nano-Glo® luciferase substrate furimazine (Promega, N1120) was added to the cells directly. The donor luminescence signal at 460 nm and acceptor emission signal at 535 nm were measured immediately using an Envision Multilabel plate reader (PerkinElmer). The $BRET^n$ signal is expressed as the ratio of light intensity measured at 535 nm over that at 460 nm. The specific $BRET^n$ signal for the interaction of two proteins is expressed as net $BRET^n$, which is defined as the difference in BRET signal with co-expression of two proteins and expression of the negative control NLuc-protein only.

The relative amount of NLuc-tagged protein expression was measured by the luminescence signal at 460 nm (L460) during the $BRET^n$ signal measurement in 1536-well white plate (Corning, 3727); while the Venus acceptor protein expression was detected by the Venus fluorescence intensity (FI) with excitation at 480 nm and emission at 535 nm in 1536-well black clear-bottom plate (Corning, 3893). Cells were seeded and transfected side-by-side under the same conditions for the 1536-well white plate for $BRET^n$ measurement and black plate for Venus FI measurement. The ratio of relative amount of acceptor over donor protein expression (Acceptor/Donor) was defined as Venus FI/L460. This intensity ratio should be proportional to the acceptor/donor ratio.

CARINA algorism for data analysis and statistics

To enable the rapid processing, quantification, and analysis of the qHT-dS data, we have developed the Comparative Analysis of Rewired INterActions (CARINA) algorithm, implemented as a Python Jupyter notebook. As the input data, CARINA directly uses the sets of raw data files generated by the plate reader in 1536-well plate format, including the $BRET^n$ PPI signals and Venus fluorescence intensity readouts. Based on the pre-designed plate templates, CARINA automatically recognizes the signals that correspond to PPI and empty vector controls for a particular bait mutated protein. For each individual PPI, CARINA computes three $BRET^n$ saturation curves, including one curve for PPI and two curves for empty NLuc (ctrl1) and Venus (ctrl2) controls, with each in four replicates. The saturation curves are based on the equation

$$Y = \frac{BRET_{max} \cdot X}{BRET_{50} + X}$$

where Y is net $BRET^n$, and X is Acceptor/Donor. The negative X and Y values were excluded from the analysis. For quantitative analysis, the area under the curve (AUC) was computed as a measurement of $BRET^n$ signal, as AUC integrates both the amplitude and shape of the saturation curve (Mo and Fu, 2016; Mo et al., 2016). The fold-over-control (FOC) was calculated as $AUC_{PPI}/AUC_{max(ctrl1, ctrl2)}$ to express the difference between PPI and empty vector controls, and statistical significance (P_{FOC}) was calculated using Student's t-test to estimate the likelihood that AUC_{PPI} is different from the $AUC_{ctrl1\&ctrl2}$.

To express the differences between the WT and MUT PPI profiles, CARINA calculates the differential score (DS) and p-value of DS (PDS) that estimate the likelihood that FOC_{WT} is significantly different from FOC_{MUT}. When WT PPI is negative and MUT PPI is positive, $DS=FOC_{MUT}$ and $PDS=P_{FOC}(MUT)$. When WT PPI is positive and MUT PPI is negative, $DS=1/FOC_{WT}$ and $PDS=P_{FOC}(WT)$. When both WT and MUT PPIs are positive, DS will be defined as FOC_{MUT}/FOC_{WT} and PDS will be calculated using Student's t-test of FOC_{WT} and FOC_{MUT}. The Benjamini-Hochberg false discovery rate (FDR)-adjusted PDS are calculated based on the Student's t-test of AUC_{WT} and AUC_{MUT} to prioritize neoPPI by considering the potential artifacts from previous statistical cut-offs.

For single dose analysis, CARINA calculates the fold over control values $FOC_{WT} = BRET_{PPI\_WT}/BRET_{max(ctrl1, ctrl2)}$ and $FOC_{MUT} = BRET_{PPI\_WT}/BRET_{max(ctrl1, ctrl2)}$, for the wild type and mutant PPI, respectively, using the BRET signals detected at the lowest DNA concentrations of the binding partners. The concentrations of the empty vector controls are matched with the binding partner concentrations based on the Venus fluorescence intensity and NLuc luminescence. Then, the Fold Change $FC_{MUT/WT}= BRET_{PPI\_WT}/BRET_{PPI\_MUT}$. The t-test p-value is calculated for the WT and MUT BRET signals obtained in quadruplicate. If $FC_{MUT/WT} > 2$ and the p-value < 0.001, the PPI is considered as the single point (SP) Go-PPI. PPIs identified as both HS-TYPE Go-PPIs and SP-Go-PPIs were prioritized as the high-confidence (HC) Go-PPIs. The CARINA analysis was implemented as a set of python scripts available on request.

Gene pathway enrichment analysis

The enrichment of the OncoPPi v2 library in cancer-associated genes has been done in python using the Enricher API (Xie et al., 2021) and based on the KEGG 2021 Human and MSigDB Hallmark 2020 gene sets.

For pathway analysis of Df-PPIs, we used a list of 125 genes that have ≥3 interaction mutation alleles. In this list, we looked for pathway category over-representation using Ingenuity Pathway Analysis (QIAGEN, Redwood City, http://www.qiagen.com/ingenuity). The analysis criteria were set as follows: (1) querying for molecules with Ingenuity Knowledge Base as a reference set; (2) restricted to human species; and (3) experimentally observed findings as a confidence level. Fisher's exact test (p-value < 0.05) was used to compute significance for over-representation of genes in a particular pathway or biological process.

Molecular biology techniques and cell culture conditions

Individual cloning vectors, site-directed mutagenesis and truncation mutants were made and verified by following product manual and standard molecular biology protocols.

Nanoluc protein-fragment complementation assay (NanoPCA)

NanoPCA was performed according to our previous publications (Mo et al., 2017). Briefly, NanoLuc-N-terminal fragment (NPN)-tagged mutant, including AKT1^{E17K}, BRAF^{V600E}, SMAD4^{G386D} and SPOP^{F133L} and C-terminal fragment (NPC)-tagged binding partners were co-transfected in the corresponding cancer cells lines. Combinations of NPN-mutant+empty NPC (ctrl1) and empty NPN+NPC-tagged binding partners (ctrl2) were used as controls respectively. PEI were used for transfection in A375, H1299 and HCT116 cells. Fugene HD (Promega, E2311) were used for transfection in MCF7 and C4-2 cells. Twenty-four hours after transfection, luminsence signal from the live cells were measured upon adding Nanoluc luciferase substrate using a BMG multi-mode plate reader (BMG PHERAstar).

GST pulldown, flag-immunoprecipitation and co-immunoprecipitation (co-IP) assays

For all the GST pulldown in HEK293T cells, cell lysate expressing GST-tagged and Venus-Flag-tagged (Venus is omitted in some figure labeling) were used. For GST pulldown and anti-flag IP assays in cancer cells, cells expressing the GST-tagged and Flag-tagged proteins were lysed in NP-40 buffer (1% nonident P-40, 20 mM Tris (PH 8.0), 137 mM NaCl, 5% glycerol, protease inhibitor (Sigma, P8340) and phosphatase inhibitor (Sigma, P5726 and P0044)) and incubated with glutathione-conjugated beads (GE,17075605) or flag-antibody-conjugated beads (Sigma, M8823) for 2 hours at 4 °C. Beads were washed three times with 1% NP-40 buffer and eluted by Laemmli sample buffer (Bio-Rad, 1610737) in GST pulldown assay and IgG elution buffer (Thermo Scientific, 21028) in Flag-IP assay. For co-IP, cell lysates were collected, quantified, and were mixed with respective antibodies. For each co-IP, lysates containing ∼1.5 mg of total proteins were used, and the antibody/lysate mixtures were incubated overnight at 4 °C. Then protein A/G agarose beads (Santa Cruz, sc-2003) were added to the mixture followed by incubation at 4 °C for another 4 hours. Beads were washed four times with lysis buffer, and proteins were eluted with IgG elutionbuffer and analyzed with indicated antibodies. Antibodies used for Western blotting are indicated in the Key Resource Table.

Venus Protein-fragment Complementation Assay (PCA)

The Venus-PCA was performed as described previously (Pham, 2015). Briefly, the cells were co-transfected with BRAF WT vs V600E and KEAP1 conjugated to C-terminal or N-terminal fragments of Venus. The cells transfected with empty vector as controls. Proteins were expressed for 48 hours, and the protein-protein interactions were monitored in live cells based on the fluorescence intensity of reconstituted Venus. The cell nuclei were stained with 5 μg/ml Hoechst 33342 (ThermoFisher, H3570) for 30 minutes at 4 °C. The cell images were taken with ImageXpress system at 447 nm (Hoechst nuclei stain) and 530 nm (Venus green fluorescence). The fluorescence intensity of reconstituted Venus was measured on the Envision spectrophotometer (Ex 485 nm and Em 535 nm, mirror 505 nm).

BioLayer Interferometry (BLI)

Direct binding studies were carried out using the Octet Red 384 system (Forte Bio), at 30 °C with shaking at 1,500 rpm in a 384-well plate containing 50 μl of the solution in each well. 1X BLI Kinetic Buffer (PBS, pH 7.4, 10 mg/ml bovine serum albumin (BSA) and 0.1% (v/v) Tween 20) was used throughout this study for protein dilution and washing steps. Ni-NTA biosensors (Sartorius, 18-5101) were balanced for the first baseline and then loaded with His-KEAP1 KELCH domain (25 μg/ml) followed by another wash for the second baseline. Kinetic analysis of the interaction was performed by dipping the sensors into the well containing recombinant human GST-BRAF WT or V600E kinase domain (200 nM).

RNA isolation, cDNA synthesis and qPCR

Total RNA was isolated using the Direct-zol RNA Mini-Prep kit (Zymo Research, R2071) following the manufacturer's instruction. cDNA synthesis was performing with the SuperScript III First-Strand Synthesis System (Life Technologies, 18080-051). Primers for qPCR analysis of gene expression are listed in the Key Resource Table. The expression of GAPDH were used as control for signal normalization.

Protein stability assays

HEK293T cells were grown in 24-well plates and transfected using FuGene (Promega, E2311) following the manufacturer's instructions. After transfection, cells were incubated for 48 hours in DMEM media supplemented with 10% FBS, then were treated with 5 μg/mL cycloheximide (Cell Signaling, 2112) in DMEM media with 10% FBS. At the indicated times, 100 μl of 2X SDS-PAGE sample buffer was added and the cells were scraped from the wells, boiled for 5 minutes, then cell lysates were stored at -80 °C. After all lysates were collected, each sample was loaded onto a 10% SDS-PAGE gel and then analyzed by Western blotting with anti-NRF2 antibody to monitor NRF2 protein level. Protein expression was quantified from the Western blot using ImageJ software for analysis, NRF2 levels were normalized to β-Actin protein levels. Assays were performed three times.

Luciferase reporter assay

HEK293T cells were grown in 6-well plates and transfected using FuGene with corresponding WT and MUT, or empty vector along with NRF2-ARE, or TCF/LEF, or AP-1 luciferase reporter plasmids (BPS Bioscience, 60514; BPS Bioscience, 60500; Qiagen, CCS-011L). Renilla luciferase was included as an internal control. After transfection, cells were incubated for 48 hours in DMEM media supplemented with 10% FBS. Cells were harvested mechanically, centrifuged at 1,600 rpm for 2 minutes, then re-suspended

Cell
Resource

 CellPress

in 300 μl of DMEM media. The cells were transferred to 384-well plate, and the reporter assay was performed using Dual-Glo luciferase kit (Promega, E2920) following the manufacturer's instructions. Firefly luciferase expression was normalized to the internal control Renilla expression. Data were analyzed with Graphpad Prism software. Assays were performed three times.

HTS cell viability assay

A pair of isogenic MCF10A cells with BRAF WT or V600E with clear genetic background was used to discover V600E cell-selective vulnerability. BRAF^{V600E} is found in 1∼3% of breast cancer patients (cBioportal), and the BRAF^{V600E}-engineered MCF10A cells recapitulates BRAF-driven tumorigenesis and dependency (Ng et al., 2018). Cells were seeded at 3000 cells/well in 50 μl media in a 384-well culture plate (Corning, Cat#3764) using a Multidrop™ Combi Reagent Dispenser (ThermoScientific) with the first column as a medium only control (blk). The next day test compounds (0.1 μl) were dispensed into wells in each plate using a Sciclone ALH 3000 liquid handler (PerkinElmer) from a compound stock plate to give the indicated final concentrations. Each sample was tested with 3 replicates. After 3 days of incubation, 10 μl CellTiter-Blue (Promega, G8081) was added to each well using the robotic liquid dispenser. The plate was incubated for 1-4 hours at 37 °C. The fluorescence intensity (FI) of each well was read using an EnVision Multilabel plate reader (Ex 545 nm, Em 615 nm, PerkinElmer). Percentage (%) of Control was calculated using the equation: (FI compound - FI Avg. Blk)/ (FI Avg. Neg. - FI Avg. Blk * 100).

QUANTIFICATION AND STATISTICAL ANALYSIS

The qHT-dS data were quantified and analyzed using the CARINA algorithm. Biochemical and biological assays were performed and repeated three times. The data quantification and statistical Student's t-test were performed using the GraphPad Prism software. See the Quantification and Statistical Details in the corresponding methods, results, and figure legends.
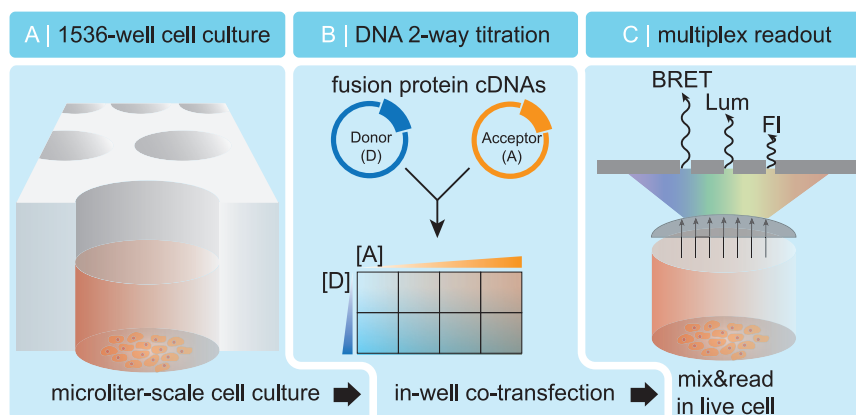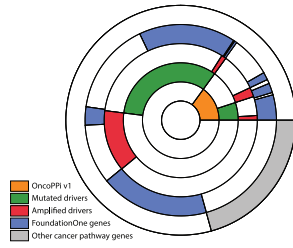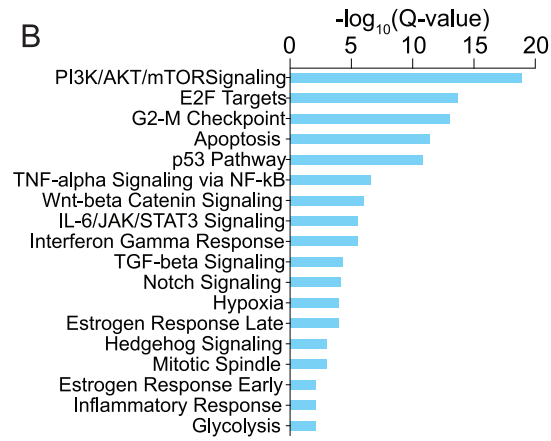
Supplemental figures

Figure S1. qHT-dS platform design and illustration, related to Figure 1B

A

- OncoPPi v1
- Mutated drivers
- Amplified drivers
- FoundationOne genes
- Other cancer pathway genes

B

-log$_{10}$(Q-value)

PI3K/AKT/mTORSignaling
E2F Targets
G2-M Checkpoint
Apoptosis
p53 Pathway
TNF-alpha Signaling via NF-kB
Wnt-beta Catenin Signaling
IL-6/JAK/STAT3 Signaling
Interferon Gamma Response
TGF-beta Signaling
Notch Signaling
Hypoxia
Estrogen Response Late
Hedgehog Signaling
Mitotic Spindle
Estrogen Response Early
Inflammatory Response
Glycolysis
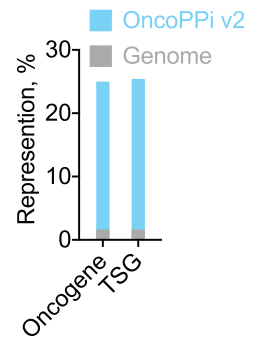
C
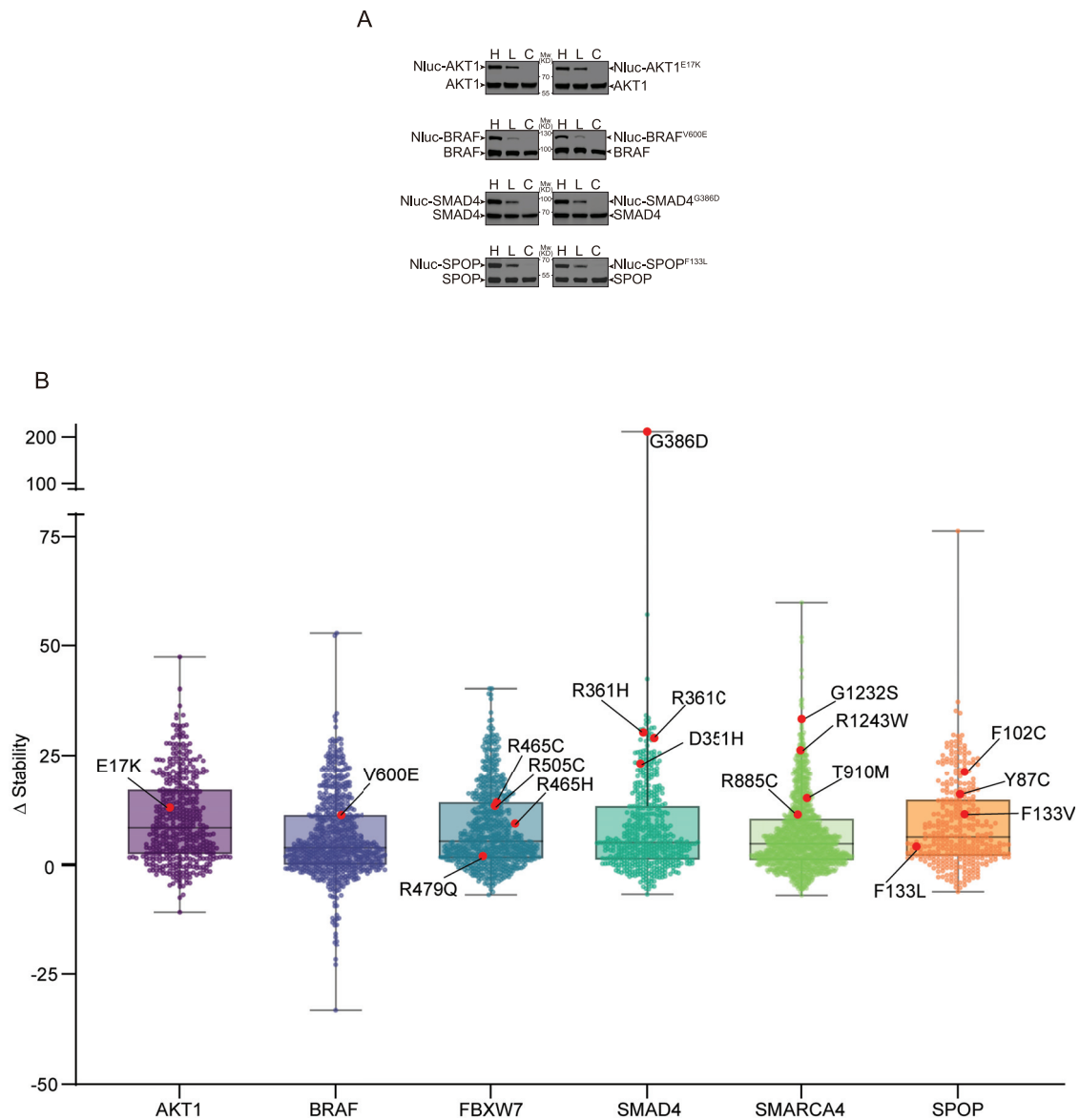

- OncoPPi v2
- Genome

Representation, %

Oncogene   TSG

Figure S2. OncoPPi v2 library design in terms of genomic alterations (A), pathway enrichment (B), and oncogenic drivers representations (C), related to Figure 1C

Figure S3. Expression and stability analysis of selected OncoMut proteins, related to Figure 3

(A) Comparison of expression between NLuc-tagged proteins and endogenous proteins. Cell lysate from HEK293T cells transfected with NLuc-tagged proteins dose dependently from high (H) to low (L) were analyzed by western blot with indicated protein antibodies. Empty NLuc vector was used as control (C).

(B) Computational prediction of mutated protein stability. The effect of point mutations on the overall protein stability has been evaluated using the Residues Scanning tool implemented in the Schrödinger software.
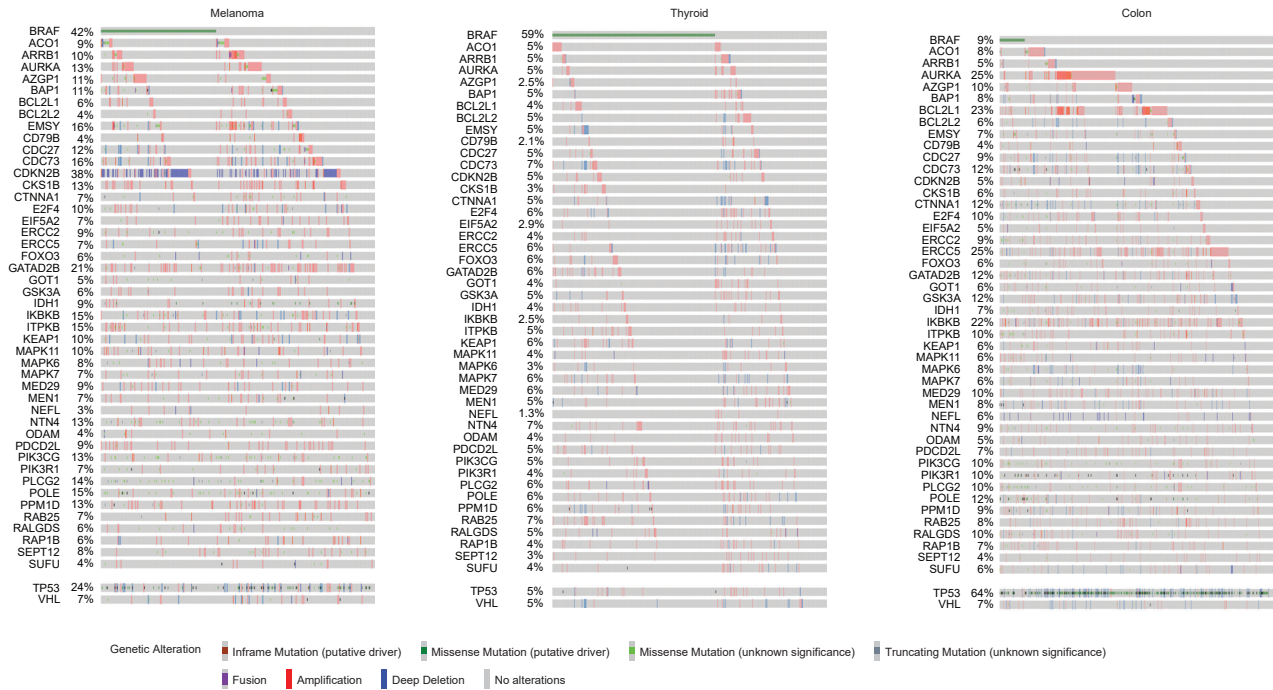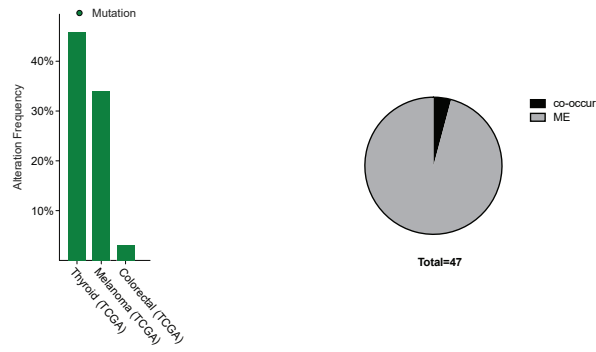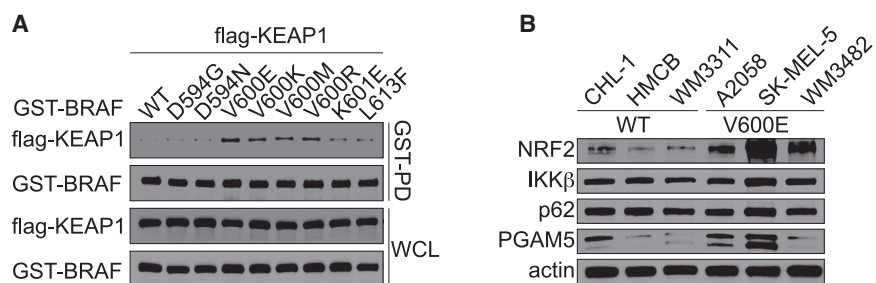
Figure S4. Mutual exclusivity analysis of BRAF^{V600E} and its neoPPI binding partners, related to Figure 4A

A

flag-KEAP1

GST-BRAF: WT, D594G, D594N, V600E, V600K, V600M, V600R, K601E, L613F

flag-KEAP1	GST-PD
GST-BRAF	
flag-KEAP1	WCL
GST-BRAF	

B

CHL-1, HMCB, WM3311, A2058, SK-MEL-5, WM3482

WT | V600E

NRF2	
IKKβ	
p62	
PGAM5	
actin	

Figure S5. Characterization of BRAF^{V600E}-KEAP1 neoPPI, related to Figures 4B and 6

(A) Comparison of the interaction between a panel of BRAF mutations with KEAP1. Cell lysate from HEK293T cells expressing GST-BRAF WT or mutations and Venus-flag-KEAP1 were subjected to GST pulldown assay and examined by western blot as indicated. related to Figure 4B.

(B) Representative blots showing protein expression of multiple known KEAP1 substrates, such as NRF2, IKKβ, p62, and PGAM5, across a panel of melanoma cells with BRAF WT or V600E genetic background.